energies

MDPI

Article

Evaluating Compressibility Assumptions for Geological CO_2 Storage Using Linear and Nonlinear Compression Evidence

Nuttapon Chaiduangsri [1], Nopanom Kaewhanam [2,*], Thammanun Chatwong [2], Sudsakorn Inthidech [3], Apichit Kampala [4], Sitthiphat Eua-apiwatch [5] and Sivarit Sultornsanee [6]

1 Department of Electrical Engineering, Faculty of Engineering, Mahasarakham University, Maha Sarakham 44150, Thailand; nuttapon.c@msu.ac.th
2 Department of Civil Engineering, Faculty of Engineering, Mahasarakham University, Maha Sarakham 44150, Thailand; 67010352002@msu.ac.th
3 Department of Manufacturing Engineering, Faculty of Engineering, Mahasarakham University, Maha Sarakham 44150, Thailand; sudsakorn.i@msu.ac.th
4 Department of Transportation, Faculty of Railway Systems and Transportation, Rajamangala University of Technology Isan, Nakhon Ratchasima 30000, Thailand; apichit.ku@rmuti.ac.th
5 Department of Civil Engineering, Faculty of Engineering, Burapha University, Chonburi 20131, Thailand; sitthiphat@eng.buu.ac.th
6 College of Engineering, Northeastern University, Boston, MA 02115, USA; s.sultornsanee@northeastern.edu
* Correspondence: nopanom.k@msu.ac.th

Abstract

Pressure buildup in geological CO_2 storage depends on how pore volume changes with effective stress, yet the laboratory evidence behind simulator compressibility inputs is often sparse. We test when a constant logarithmic compression slope is adequate and what the choice changes in a caprock screen. An exact minimax bound identifies loading intervals where a constant slope must fail. Arc Joint via Optimum Parameters (AJOP) and five competitors were fitted to 19 published trajectories with trajectory-level statistics, information criteria and bootstrap tangent uncertainty, and an independent-specimen cohort was ranked before and after a pre-declared exclusion. Caprock laws based on two unloading moduli measured on one Draupne specimen were run in OPM Flow on a layered model and the published Smeaheia simulation model. AJOP5 gave a median range-normalized RMSE of 1.27% (95% CI 0.81–1.74%); the quadratic gave 0.26% but reversed in four cases. The curvature term was unsupported in 12 fits, and tangent-slope uncertainty reached 123%. High-stress rankings reversed after exclusion. The caprock law changed reservoir buildup by at most 19% but caprock pressure by up to 59% (layered model) and changed no screening class. The bound applies to primary loading only, and small curve errors do not ensure reliable tangent properties.

Keywords: geological CO_2 storage; compressibility; effective-stress interval; AJOP; caprock unloading; coupled flow–geomechanics; OPM Flow; pressure screening

Check for updates

Academic Editor: Nikolaos Koukouzas

Received: 12 October 2026
Revised: 5 November 2026
Accepted: 6 November 2026
Published: 7 November 2026

Copyright: © 2026 by the authors. Licensee MDPI, Basel, Switzerland. This article is an open access article distributed under the terms and conditions of the Creative Commons Attribution (CC BY) license.

1. Introduction

Geological CO_2 storage assessments must show that pressure buildup remains compatible with containment and with the intended injection operation [1–6]. Compressibility enters this assessment through pore-volume change and skeleton deformation, both governed by effective stress [7–10]. At approximately fixed total stress, rising pore pressure unloads the skeleton, whereas lateral constraint, pressure gradients and thermal contraction produce other paths elsewhere in the reservoir–caprock system [10–16]. In Frio sand,

Zheng and Espinoza [17] measured different pore-volume compressibilities for loading and unloading, and an inappropriate value underestimated injection-induced pressure buildup in their simulations; the calibration path is therefore part of the property specification. Field observations at In Salah, Sleipner, and Weyburn show that geometry, pressure communication and rock properties control deformation [15,18–20], induced-seismicity assessments depend on the initial stress state and the pressure change [21–23], and pressure management can be part of the integrity strategy [24]. The adequacy of a compressibility assumption must therefore be judged against the accuracy required of the engineering output.

Three bodies of work bear on that judgement. The first is storage modeling. Reservoir simulators accept stress-dependent pore-volume tables and coupled geomechanical modules, but the table entries must still come from laboratory or field evidence, and when that evidence is sparse, constant values are assigned. In the Smeaheia archive, three constant pore-volume compressibilities spanning two orders of magnitude produced markedly different pressures [25–27], and Wang et al. [28] quantified storage-efficiency uncertainty on the same dataset; thermal effects, uncertain properties, the loading rate, coupling and nonlinear elasticity add further uncertainty [16,29–32]. Coupled reservoir–geomechanical analysis is well established, from multilayer reservoir–caprock systems [14] and the In Salah injection [15,19] to cross-site comparisons [20], reviews [10], coupled subsidence assessment [31] and a three-dimensional geomechanical model of Smeaheia [25], and open-source simulators now couple multiphase flow with poroelastic mechanics [33–35]. Every such model, however, takes its compressibility or stiffness law, or the tabulated equivalent, as an input.

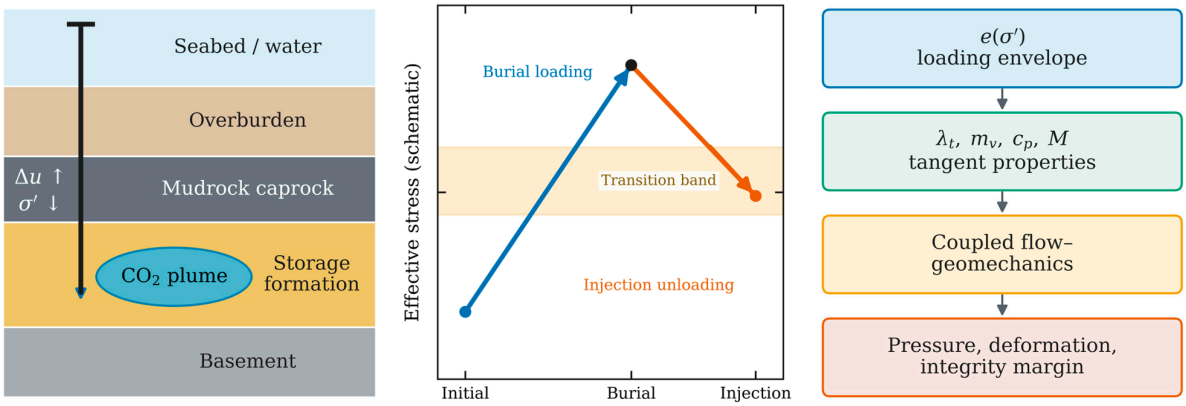
The second body of work concerns what that input means. A logarithmic void-ratio slope, a constrained compressibility, a pore-volume compressibility and a constrained modulus are related but not interchangeable, and a straight line in the void ratio against log stress does not imply constant stiffness. Lee et al. [36] linked measured pore and bulk compressibilities to analytical estimates of storage efficiency and deformation, and rate effects, nonlinear shale response and pore-structure change introduce further distinctions [30,32,37–39]. Clay-rich sediments range from nearly linear to strongly curved over laboratory stress windows, depending on fabric, bonding, stress history, mineralogy and porosity [40–46]; resedimented mudrocks isolate composition from natural structure [47–51], and preferred compression relations differed among 15 resedimented materials [48]. The Arc Joint via Optimum Parameters (AJOP) family, which grew from the square-root transition of Kaewhanam and Chaimoon [52], was developed for clay consolidation by Phonchamni et al. [53] and used in AJOP-T hardening by Chatwong et al. [54], providing a common setting for this range: it represents a curve approaching a straight branch and contains an exact straight-line member. Its nonnegative slope-contrast form has a nonincreasing void-ratio derivative in log stress, so a slightly concave-up response is approximated by the linear member with its error reported. The material state and loading branch remain separate limits: an intact bonded sediment, a resedimented mixture and an unloading path need not share one envelope [40–42,55,56].

The third body of work concerns how such evidence is tested. Complete-window residuals describe representation, stress-blocked tests address prediction, and parameter diagnostics address identification [57,58]; material change, including geochemical alteration, further limits transfer [59]. An accurate curve can have an inaccurate derivative, and a plausible range of property values does not establish that a constitutive form or calibration window supports the intended use. Open data now allow these levels to be separated: loading trajectories of resedimented Nankai mixtures [60], incremental-loading records from Sites C0011 and C0012 [61], and sediment–diatom mixtures [62,63]; independent Boston Blue Clay specimen endpoints [64]; an intact Draupne oedometer record [65,66]; and archived Smeaheia pressure scenarios with a released site simulation model [26,27].

These strands do not meet. Coupled models propagate whatever law they are given, laboratory studies compare curve fits, and storage uncertainty analyses vary assigned property ranges, but none asks when a constant compressibility assumption changes a containment screen and what laboratory evidence is needed to decide. This study addresses that question with three contributions:

- An exact minimax bound that identifies primary-loading intervals on which no constant logarithmic slope can meet a stated tolerance (Section 2.3);
- Representation, prediction and identification tests of constant and nonlinear compression laws on published laboratory data, with trajectory-level statistics, bootstrap tangent uncertainty and independent-specimen rankings before and after a pre-declared exclusion (Sections 3.1–3.4);
- A route that carries the loading envelope and a measured unloading branch through simulator tables into a coupled layered model and the published Smeaheia simulation model (Sections 2.6, 3.5 and 3.6).

The three tests are complementary; they do not form a single laboratory-to-reservoir validation chain. Figure 1 places the assessment within the storage problem.



(**a**) (**b**) (**c**)

Figure 1. Conceptual propagation of a compressibility assumption through a geological CO_2-storage assessment. (**a**) Injection raises pore pressure in the storage formation and changes the effective-stress path in the reservoir and caprock. (**b**) Burial is represented as primary loading, whereas a pore-pressure increase at approximately fixed total stress produces unloading; the transition band belongs to the loading envelope and is not used as an unloading law. (**c**) The constitutive relation supplies tangent quantities to the coupled model, which propagates them to pressure, deformation, and integrity outputs. The figure is conceptual and contains no Smeaheia simulation result.

2. Materials and Methods

2.1. Data Sources and Unit of Analysis

The trajectory benchmark contains 19 loading trajectories grouped by source. P01–P06 are six resedimented Nankai mixtures from Reece et al. [60]; P07–P11 are five incremental-loading records from Hüpers and Kopf [61], four natural silty clays and one remolded sample (P08); and P12–P19 are eight resedimented Boston Blue Clay (BBC) and Eugene Island (EI) mixtures with lacustrine or marine diatomaceous earth (LDE, MDE) from Scott and Reece [62,63]. The source register in Supplementary File S1 gives specimen identifiers, workbook sheets, columns, units, extraction rules and file hashes. These materials broaden the curve-shape comparison; they are not treated as site-specific storage rocks. The trajectory is the unit of analysis: points within a trajectory are not independent replicates, so medians, bootstrap confidence intervals over trajectories and paired Wilcoxon tests are computed across the 19 trajectories, and generality is checked by leaving one source out at a time.

For the fourteen continuous trajectories, the void ratio was interpolated linearly in log stress at the frozen evaluation locations. The six Nankai windows span 0.2–20 MPa and the eight Scott–Reece windows span 0.2–1.8 MPa, with 40 derived locations per curve. The five incremental-loading curves retain 9 or 10 source endpoints spanning 0.12–16 or 20 MPa. All locations in these windows enter the full-data fit. The continuous measurements are also shown as pale background traces in the figures. Derived locations are numerical evaluation points, not additional experiments or independent replicates.

The storage evidence is the official Smeaheia reference archive [26] and the associated field-scale study [25]. The pressure benchmark is Table 5-2 of the Troll Kystnær Subsurface Status Report, revision 03 (2012) [27]. It reports pressure buildup after 50 years of 3.2 Mt yr^{-1} injection for three pore-volume compressibilities and four connected-volume cases. The twelve values and the compressibility inputs in Section 5.1 of the source report [27] were checked directly against that report and transcribed into the machine-readable table. The archive is used only as the compressibility benchmark; the simulations of Sections 2.6, 3.5 and 3.6 are new.

The official report evaluated pore-volume compressibilities of 1.6×10^{-6}, 4.0×10^{-5}, and 1.6×10^{-4} bar^{-1} because no Smeaheia laboratory constraint was available [26,27]. Connected water volumes were 51, 160, 297, and 418 GSm^3. The present analysis preserves the twelve reported pressure outcomes and compares all twelve cases with the updated report screens, evaluated at 900 m TVDmsl, of 33 bar for a caprock containing pre-existing fractures and 65 bar for intact Draupne shale.

The original pressure table was color-coded against an earlier 20 bar criterion. The present classifications are recalculated from the archived pressures using the later assessment in Section 4.7 of the same report: 33 bar in its narrative summary (33.1 bar in Table 4-2) for the base minimum-stress case and 65 bar for the low-case intact-rock fracture-initiation model. Neither screen includes thermal stress effects [27].

2.2. Compression Laws and Tangent Quantities

For one-dimensional constrained compression, effective vertical stress is written as

$$\sigma'_{\mathrm{v}} = \sigma_{\mathrm{v}} - \alpha p, \tag{1}$$

where σ_{v} is total vertical stress, p is pore pressure, and α is Biot's coefficient [7–9]. Compression is taken as positive. The distinction among commonly conflated properties is

$$\lambda_{\mathrm{t}} = -\frac{\mathrm{d}e}{\mathrm{d}\ln\sigma'_{\mathrm{v}}}, \qquad m_{\mathrm{v}} = \frac{\mathrm{d}\varepsilon_{\mathrm{v}}}{\mathrm{d}\sigma'_{\mathrm{v}}}, \tag{2}$$

and

$$c_{\mathrm{p}} = -\frac{1}{V_{\mathrm{p}}}\frac{\mathrm{d}V_{\mathrm{p}}}{\mathrm{d}\sigma'_{\mathrm{v}}}. \tag{3}$$

Here, λ_{t} is the local logarithmic compression slope, m_{v} is constrained compressibility, c_{p} is pore-volume compressibility, ε_{v} is compressive logarithmic volumetric strain, and V_{p} is pore volume. The derivative in Equation (3) is defined with respect to effective vertical stress along the constrained laboratory path. A reservoir ROCK input refers to pore-volume response under the simulator's pressure and stress assumptions; it is not obtained from Equation (3) without specifying those assumptions. Let V_{s} denote the constant solid volume. Assuming incompressible solids and one-dimensional strain, $V_{\mathrm{p}} = eV_{\mathrm{s}}$ and $V = (1+e)V_{\mathrm{s}}$. The exact logarithmic strain relative to a reference state is

$$\varepsilon_{\mathrm{v}} = \ln\left(\frac{1+e_0}{1+e}\right). \tag{4}$$

These definitions prevent a constant λ_t, a constant m_v, and a constant c_p from being treated as equivalent null models. Here, e_0 is the void ratio at the strain-reference state; it is distinct from the transition-state parameter e_r introduced below. A logarithmic stress derivative means differentiation with respect to the logarithm of stress divided by a fixed positive reference stress.

Starting from the AJOP family [52–54], let

$$u = \ln\left(\frac{\sigma'_v}{p_r}\right), \tag{5}$$

where $p_r > 0$ is the transition stress. Define $\Delta\lambda = \lambda_\infty - \lambda_0$ and the centered transition function:

$$g(u) = u + \sqrt{\theta_c + u^2} - \sqrt{\theta_c}. \tag{6}$$

The centered AJOP-family loading envelope is

$$e(\sigma'_v) = e_r - \lambda_0 u - \frac{\Delta\lambda}{2} g(u). \tag{7}$$

The centering term $-\sqrt{\theta_c}$ is essential: it makes $e_r = e(p_r)$. Without it, e_r cannot be interpreted as the void ratio at the transition stress. The remaining parameters are the low-stress slope λ_0, high-stress slope λ_∞, and positive dimensionless transition-width parameter θ_c. For monotonically increasing compression slope, the admissible ordering is $0 \le \lambda_0 \le \lambda_\infty$. With a zero low-stress slope, Equation (7) recovers the earlier four-parameter shape after centering and parameter rescaling.

The physically admissible loading domain is restricted to positive effective stress and a positive void ratio. The asymptotic slopes are mathematical limits of the model; they do not imply physical validity at arbitrarily large stress.

Differentiation gives the local slope

$$\lambda_t(u) = \lambda_0 + \frac{\Delta\lambda}{2}\left(1 + \frac{u}{\sqrt{\theta_c + u^2}}\right), \tag{8}$$

and its evolution with log stress

$$\frac{d\lambda_t}{du} = \frac{\Delta\lambda}{2} \frac{\theta_c}{(\theta_c + u^2)^{3/2}}. \tag{9}$$

For $\Delta\lambda > 0$, p_r is exactly the stress at which the slope is halfway between its asymptotes, and the maximum rate of slope change is $(\lambda_\infty - \lambda_0)/\left(2\sqrt{\theta_c}\right)$ at $\sigma'_v = p_r$. The stresses at which 10% and 90% of the slope transition have occurred define an exact transition band,

$$\sigma'_{10,90} = p_r \exp\left(\mp \frac{4\sqrt{\theta_c}}{3}\right). \tag{10}$$

The minus sign gives σ'_{10} and the plus sign gives σ'_{90}. This band locates the central part of the loading-slope transition. Intersecting $\left[\sigma'_{10}, \sigma'_{90}\right]$ does not alone prove failure of a constant; the slope contrast over the actual interval must be tested. When $\Delta\lambda = 0$, the slope is constant and no distinct 10–90% transition band can be identified; Equation (10) is then not a transition diagnostic.

For incompressible solids, the derivative-consistent quantities passed to a constrained geomechanical calculation are

$$\begin{aligned} m_v(\sigma'_v) &= \frac{\lambda_t}{(1+e)\sigma'_v}, \\ c_p(\sigma'_v) &= \frac{\lambda_t}{e\sigma'_v}. \end{aligned} \tag{11}$$

The tangent constrained modulus is

$$M(\sigma'_{\mathrm{v}}) = \frac{1}{m_{\mathrm{v}}} = \frac{(1+e)\sigma'_{\mathrm{v}}}{\lambda_{\mathrm{t}}}. \tag{12}$$

Equations (11) and (12) show why even an asymptotically constant λ_{t} does not imply constant m_{v}, c_{p}, or M. Equation (12) requires $\lambda_{\mathrm{t}} > 0$. If the slope vanishes, constrained compressibility is zero and the modulus is understood as an infinite-stiffness limit.

Six forms are compared on every trajectory: the constant logarithmic slope (log-linear), a quadratic in log stress, a quadratic constrained to remain monotone and positive over the fitted interval, the positive-exponent curved-function (CF) power relation of Phonchamni et al. [53], AJOP4 and AJOP5. The CF exponent ranges from zero, the logarithmic limit, to five, so the CF form is distinct from the quadratic in log stress. The monotone quadratic is constrained at both interval endpoints on its derivative and at the upper endpoint on the void ratio; because its derivative is linear, these inequalities enforce monotonicity throughout the interval. The single-specimen and cohort analyses (Section 2.5) use the following baselines:

1. A constant log-slope relation, $e = e_* - \lambda_{\mathrm{c}} \ln(\sigma'_{\mathrm{v}}/\sigma'_*)$;
2. A constant constrained-compressibility law, $1 + e = (1 + e_*) \exp\left[-m_{\mathrm{v,c}}(\sigma'_{\mathrm{v}} - \sigma'_*)\right]$, where the starred stress and void ratio specify the same reference state, and the constant constrained compressibility is positive;
3. The nested AJOP form obtained from Equation (7) by setting $\lambda_0 = 0$;
4. The published five-parameter empirical mudrock model of Uyeturk and Germaine [50].

The constant-logarithmic-slope baseline is the normal-compression line of Cam-clay-type critical-state models [67], so the linear AJOP member is the critical-state benchmark in one-dimensional compression. Reversal-referenced unloading stiffness, as in bounding-surface models such as MIT-S1 [68], belongs to the unloading branch (Section 2.6). A full critical-state simulation is not attempted, because one-dimensional compression data cannot constrain the shear parameters.

2.3. An Exact Failure Bound for a Constant Slope

Suppose the stress domain is broad enough to sample both asymptotic slopes and $0 < \lambda_0 < \lambda_\infty$. Minimizing the maximum absolute relative slope error over the two limiting values gives

$$\lambda_{\mathrm{c}}^* = \frac{2\lambda_0\lambda_\infty}{\lambda_0 + \lambda_\infty}, \qquad E_{\min} = \frac{\lambda_\infty - \lambda_0}{\lambda_\infty + \lambda_0}. \tag{13}$$

Here, λ_{c}^* is the minimax constant and $E_{\min}$ is its unavoidable worst-case relative error at the two asymptotes. For an allowable relative slope error τ with $0 < \tau < 1$, no constant slope can satisfy the tolerance across both regimes if

$$\frac{\lambda_\infty}{\lambda_0} > \frac{1+\tau}{1-\tau}. \tag{14}$$

At $\tau = 0.10$, failure is guaranteed when $\lambda_\infty/\lambda_0 > 11/9 \approx 1.222$. If $\lambda_0 = 0$, a relative bound is undefined and the minimum maximum absolute slope error is $(\lambda_\infty - \lambda_0)/2$. Equations (13) and (14) are constitutive bounds; storage-scale failure still requires propagation to an engineering output.

For the positive-slope case, restrict the candidate constant to the interval between the two slopes: a value outside it cannot reduce the maximum error. At the minimizer, its relative overprediction at the lower slope equals its relative underprediction at the higher slope. Solving this equality gives the harmonic mean in Equation (13). For any intermediate slope, the absolute relative error is no greater than the larger endpoint error, which proves the minimax result. On a finite stress interval, the same argument applies exactly to the

minimum and maximum local slopes on that interval; the asymptotic values should be used only when they are justified.

Scope. Equations (13) and (14) bound the slope of the primary-loading envelope only. They do not apply to injection-induced unloading or to reloading, which follow different branches with different stiffness. Unloading must be represented by a separately measured branch (Sections 2.5 and 2.6).

Equations (10)–(14) separate the location of a slope transition from a proof that a constant fails. The 10–90% band locates the central transition, but crossing that band is not a sufficient failure criterion. For any specified interval with positive slopes, Equation (13) applies with its actual minimum and maximum slopes. A constant is excluded at tolerance τ only when their ratio exceeds $(1+\tau)/(1-\tau)$. The asymptotic form in Equation (14) is the limiting result when both asymptotes are represented. Figure 2 shows these dataset-independent relationships.

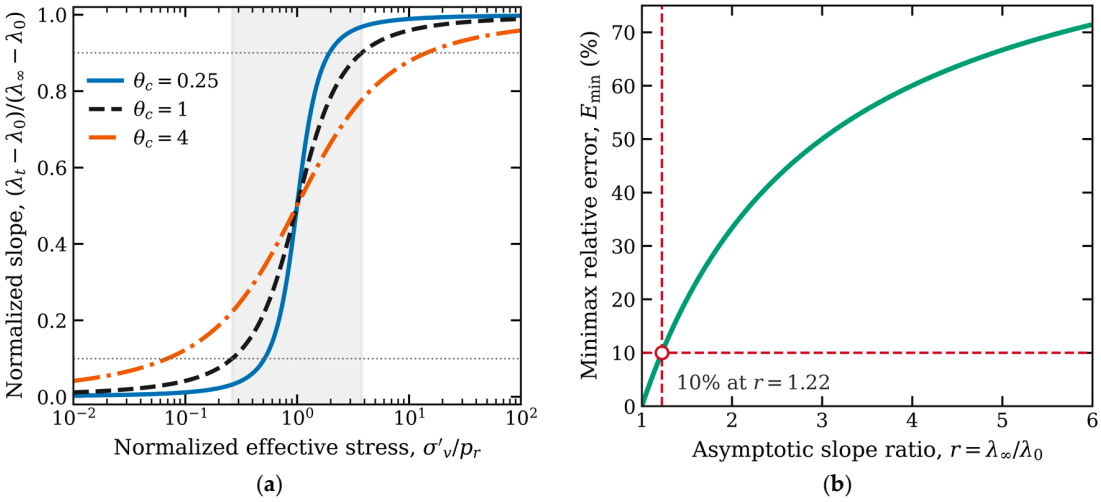


Figure 2. Dataset-independent consequences of Equations (8), (10), (13), and (14). (**a**) Normalized local-slope transition versus normalized effective stress for three transition-width parameters; the shaded interval is the exact 10–90% band for $\theta_c = 1$. (**b**) Unavoidable minimax relative error of a constant slope as a function of the asymptotic slope ratio $r = \lambda_\infty/\lambda_0$; the dashed lines mark a 10% tolerance and its critical ratio $r = 11/9 \approx 1.222$. The figure contains analytical results only and no fitted data.

The bound also explains why the calibration window matters. A constant fitted at low stress overpredicts stiffness after the slope has increased, a high-stress constant underpredicts it at low stress, and a secant fitted across the full window can reduce void-ratio residuals while retaining biased tangents at both ends. At a common stress and void ratio, the relative errors in constrained and pore-volume compressibility equal the relative error in the local logarithmic slope; if competing models predict different void ratios, the void-ratio denominators also enter the tangent-property errors.

2.4. Calibration, Prediction and Evaluation Criteria

The centered AJOP5 family includes a globally linear member when $\Delta\lambda = 0$. Equation (7) then becomes

$$\Delta\lambda = 0 \Rightarrow e = e_r - \lambda_0 u \tag{15}$$

The four-parameter member has $\lambda_0 = 0$. Its zero-curvature limit $\theta_c = 0$ gives a horizontal branch below the reference stress and a straight descending branch above it. Over a window entirely on the descending branch,

$$e = e_r - \Delta\lambda u, \text{ for } u \geq 0, \quad \lambda_0 = 0, \quad \theta_c = 0 \tag{16}$$

This is the linear limit of Phonchamni et al. [53] in the present centered coordinates. A zero curvature parameter produces a sharp corner if the transition lies inside the window; to fit a wholly linear window, the reference stress is fixed at the lowest observed stress, so the line has two effective parameters and its unobserved transition location is not estimated. A boundary solution therefore indicates lack of data support for curvature, not proof of zero curvature.

AJOP estimation profiles out the linear coefficients by bounded conditional least squares and searches the two shape coordinates. The reference stress remains within the observed calibration window; the smooth curvature parameter ranges from 0.0001 to 100. Linear coefficients lie between zero and the larger of 2 and twice the maximum observed void ratio. An 81 by 81 shape grid, 24 local starts, and four differential-evolution seeds provide independent numerical checks. The exact linear candidates in Equations (15) and (16) are included explicitly. A linear boundary is selected only when its squared-error objective is no greater than the smooth optimum to numerical precision. No general zero-curvature kink is fitted in this benchmark.

The previous primary stress blocks are preserved separately. For continuous curves, 25 lower-stress locations formed calibration and 15 higher-stress locations formed prediction; cutoffs were approximately 5 MPa for P01–P06 and 0.8 MPa for P12–P19. For P07–P11, the first seven endpoints through 8 MPa formed calibration, leaving two or three higher-stress endpoints. Bounds and fitting inputs were obtained from those training windows. These blocked comparisons, alternative cutoffs, and interior holdouts are retained unchanged in S1 and S2. The full-window extension is exploratory and uses responses that were withheld in those earlier tests; it is not a new prospective validation.

Every comparison minimizes the same unweighted sum of squared void-ratio residuals at the same locations. Full-data error measures representation over the fitted interval, held-out error measures prediction under a stated partition, and information criteria and sensitivity diagnostics address identification [57,58]; a lower calibration error does not establish parameter identification.

Table 1 separates approximation, prediction, identification, tangent properties, and engineering consequence. For the 19-trajectory full-data analysis, RMSE and maximum absolute error are normalized by the observed void-ratio range of each complete evaluation window. The 1%, 2%, and 5% RMSE levels are illustrative sensitivity bands, not independently justified acceptance limits. They were examined during this exploratory re-analysis. A project-specific tolerance must instead follow the error permitted in the intended engineering output.

Fit residuals were propagated to the tangent slope λ_t and the pore-volume compressibility c_p by a residual moving-block bootstrap with $B = 1000$ resamples per trajectory (block length 5 for trajectories with more than 12 points, 1 otherwise). The relative half-width of the 95% percentile interval is reported on 41 logarithmically spaced stresses inside the observed window.

Table 1. Separate criteria for representation, prediction, identification, and transfer.

Level	Quantity	Evaluation Criterion
Representation	Complete-window void ratio	Report RMSE and maximum pointwise error relative to the observed range, both per trajectory. RMSE levels of 1%, 2% and 5% are descriptive counts only and are not linked to field thresholds. Propagate residuals to λ_t and c_p by residual bootstrap. Verify positivity and monotonicity inside the window; report tangent properties only inside the observed window.
Prediction	Held-out e and local λ_t	For held-out e, flag error above 10% of the observed held-interval change. For a slope approximation, test the maximum relative slope error over the specified interval. Report absolute error and processing sensitivity.
Identification	p_r and nonlinear parameters	Interpret physical parameters only when training information sensitivity, profile diagnostics, and physical predictions support them. An undefined AIC_c indicates inadequate information for that criterion; it does not alone prove non-identification.
Tangent property	m_v, c_p, or M	Flag a maximum relative difference above 10% over the stated path; retain the physical definition.
Engineering	Pressure or integrity margin	Flag a decision as non-robust when the documented property range changes the 33 or 65 bar Smeaheia classification.
Transfer	Material state and branch	Do not transfer primary-loading or off-site values without an explicit sensitivity bound.

Normalization by the observed range supports within-curve comparison but does not measure relative error in void ratio, stress, settlement, or stiffness. The tangent-property screening tolerance likewise is not a regulatory threshold.

2.5. Single-Specimen and Independent-Specimen Cohorts

The laboratory evidence is the open replication dataset for the Draupne shale test program [65,66]. The oedometer specimen was cut normal to bedding, had an initial height of 20.34 mm and diameter of 50.35 mm, and had a reported initial porosity of 18.92%. The repository file contains 22,724 chronological observations of elapsed time, vertical strain, pore pressure, and effective vertical stress. The SHA-256 hashes, original filenames, and processing environment are recorded in Supplementary File S1. All Draupne results therefore rest on a single specimen, cored in well 16/8-3S in the Ling Depression rather than at Smeaheia [65].

Stable endpoints were defined as the median of the final 60 min of each documented hold. The six successive primary-loading maxima were 10.98, 15.00, 22.49, 33.76, 50.63, and 75.96 MPa. The chronology also contained unloading from 33.76 to 22.49 MPa, reloading to 33.76 MPa, and final unloading through 50.62, 33.75, and 22.48 MPa. These windows measure endpoint repeatability; they do not represent specimen-to-specimen uncertainty.

The reported strain is engineering vertical strain in millistrain. With one-dimensional deformation and incompressible solids, a reference-shifted void ratio was reconstructed from $e = e_{ref} - (1 + e_{ref})\varepsilon_{eng}$. The reported 18.92% porosity gives $e_{ref} = 0.23335$, which was assigned to the first stable endpoint because the strain channel is effectively zero there. Here, ε_{eng} is the engineering strain relative to that first endpoint. For the reconstruction, $e_0 = e_{ref}$ in Equation (4), so $\varepsilon_v = -\ln\left(1 - \varepsilon_{eng}\right)$. This convention fixes both the void-ratio offset and the conversion factor from engineering strain to the void ratio. The measured engineering-strain increments are unchanged by that choice, whereas absolute void-ratio increments

and errors scale with one plus the assigned reference void ratio. For this reconstruction, the logarithmic strain depends only on the measured engineering strain.

The independent-specimen evidence was transcribed from Table 5-1 of Casey's open doctoral thesis [64] (p. 153). Each row identifies a separate resedimented Boston Blue Clay triaxial specimen and reports its terminal pre-shear state; ideal K_0 consolidation is not assumed for every specimen. The primary cohort retained OCR = 1 specimens with a finite effective vertical stress and void ratio and excluded the three tests flagged in the source as having high excess pore pressure during consolidation. Thirteen specimens remained, spanning 0.198–101.25 MPa. These values are terminal states from separate preparations, not repeated observations along one continuous curve. The complete 27-row transcription, source-row notes, and inclusion flags are preserved in Supplementary File S1.

The Draupne analysis evaluated six models in void-ratio space: constant logarithmic slope; constant constrained compressibility; a quadratic in log stress; the nested form of Equation (7) with $\lambda_0 = 0$; the unrestricted five-parameter transition law; and the five-parameter Uyeturk–Germaine relation [50]. The RBBC specimen-level screen evaluated the same two constant models, the quadratic, and both five-parameter laws. All models used unweighted void-ratio residuals. The exponential constant constrained-compressibility relation follows from Equations (2) and (4). Linear regression of $\ln(1 + e)$ against effective stress supplied only its initial guess; the final parameters minimized unweighted squared residuals in e, using an analytical Jacobian. Thus, the response transformation did not change the fitting objective relative to the competitors.

For the Draupne and RBBC analyses, nonlinear models were estimated by bounded least squares with deterministic multistart initialization. For the transition law, $0 \leq e_r \leq 1, \lambda_0$, and $\Delta\lambda$ were non-negative, p_r was restricted to the fitted stress interval, and $10^{-4} \leq \theta_c \leq 100$. Ninety starting points were used for the principal Draupne fits. For RBBC, full-data fits used 32 starts, blocked-training fits used 40, and leave-one-specimen-out refits used 32 starts constructed solely from each training fold. No fit to the complete dataset supplied a cross-validation starting point. Stress-dependent bounds in blocked and leave-one-out fits were also obtained only from the training observations. For the Uyeturk–Germaine comparator, the offset is subtracted and may be signed; positivity of the infinite-stress void ratio is not imposed. Its finite fitting bounds are study-specific. Supplementary File S1 documents the source-equation convention, parameter mapping, seeds, bounds, and transformed parameterizations.

Model diagnostics were root-mean-square error (RMSE) and mean absolute error in the void ratio, leave-one-out cross-validation for the three low-order models, the corrected Akaike information criterion (AIC_c) [57], and the Bayesian information criterion [69]. For the AIC_c, the fitted residual variance was counted as a parameter. AIC_c was reported as undefined when $n - K - 1 \leq 0$, where K includes that variance term. This rule prevents a nearly saturated five-parameter fit to six endpoints from being presented as information-criterion evidence. The AIC_c and BIC use the Gaussian residual score with the common additive constant omitted. These are descriptive comparisons under a working independent equal-variance error model, not tests of physical identification. The nominal five-parameter score is not interpreted for the RBBC transition fit because collapse to a constant slope makes its parameterization singular.

Practical identifiability was evaluated from the column-scaled local sensitivity matrix and by profile likelihood [58]. The transition stress p_r was fixed at 64 logarithmically spaced values from 10.98 to 75.96 MPa while the remaining parameters were reoptimized. A nominal 95% likelihood-ratio threshold was plotted for diagnosis. Because the unrestricted fit has only one residual degree of freedom, this threshold is not treated as a population confidence interval. Nominal 95% t-based intervals were calculated for the two-parameter

constant models; the constant-compressibility interval used a local Jacobian linearization of its nonlinear least-squares fit. These intervals are conditional on the working residual model and do not quantify between-specimen uncertainty. Three further definitions are used. The identifiable combination is the eigenvector of the weakest scaled-sensitivity direction. A boundary hit is a parameter at its bound within a stated tolerance. The multistart protocol combines four differential-evolution runs per trajectory with local starts, and the share of runs converging to the best objective is reported.

The tail holdout used a fixed stress-based partition. The first five primary-loading endpoints, from 10.98 to 50.63 MPa, were used for calibration, and the 75.96 MPa endpoint was predicted without refitting. Absolute error in the void ratio was reported together with the error as a percentage of the observed void-ratio change from 50.63 to 75.96 MPa. A model with p parameters was not assigned a holdout result when the number of calibration observations was no greater than p. Under this rule, neither five-parameter law can be validated by a five-point calibration even if an optimizer returns a number. With residual variance counted, the AICc is defined only for $p \leq 3$ at $n = 6$; five-parameter fits are therefore reported as identifiability diagnostics, not as competing models.

The complete calculation was repeated with 30, 60, and 120 min endpoint windows. A result was regarded as processing-stable when its interpretation did not change across these windows. Local slopes were calculated only between stable raw-data endpoints; no numerical derivative of a digitized curve was used. For adjacent endpoints, interval properties are $\lambda_{sec} = -\Delta e / \Delta \ln(\sigma'_v / p_r)$ and $M_{sec} = \Delta \sigma'_v / \Delta \varepsilon_v$, with any fixed positive p_r in the logarithmic difference. They are secants, not pointwise tangents.

The specimen-level high-stress block used a fixed 10 MPa threshold. Ten specimens consolidated at $\sigma'_v \leq 10$MPa formed the calibration cohort, and three specimens above 10 MPa formed the test cohort. Because the 10 training specimens exceed $p = 5$, both five-parameter laws could be evaluated out of sample. This count permits a numerical prediction; it does not by itself establish parameter identification. The full-data RMSE, AIC_c, BIC, leave-one-specimen-out (LOSO) RMSE, and blocked high-stress RMSE were reported separately.

An exclusion rule was declared before the re-analysis but after the original results had been seen; the time-stamped record is in Supplementary File S3. A specimen is excluded if the source declares its response erroneous or if K_0 conditions are not demonstrated (K_0 not reported, or not strictly between 0 and 1). The rule excludes TX1030 (response declared erroneous by the source), TX1124 ($K_0 = 1.0$) and TX1147 (K_0 not reported), leaving a screened cohort of 10 specimens, 7 for calibration and 3 test specimens above 10 MPa. The 13 primary endpoints form a cross-sectional envelope whose scatter includes preparation and apparatus effects, so leave-one-specimen-out RMSE is the primary predictive metric and full-data RMSE is secondary.

Cohort sensitivity was evaluated with two explicit alternatives. A strict-K cohort also required $0 < K_0 < 1$ and retained 11 specimens. An inclusive cohort reinstated the three source-flagged high-excess-pore-pressure tests and retained 16 specimens. An additional source-audit sensitivity excluded TX1030 because Casey identifies its stress-ratio response as erroneous [64] (p. 149); this left 12 specimens, with nine for training and three for the blocked test. The primary cohort was retained because the source warning does not specifically invalidate its endpoint stress or void ratio. No derivative was estimated from these discontinuous specimen endpoints. The test therefore evaluates the prediction of the terminal void ratio within one resedimented material, not a continuous constitutive trajectory or transfer across mudrocks.

Equation (7) is a primary-loading envelope and was not used for unloading. Secant moduli were calculated separately for the observed first unloading, reloading, high-stress

unloading and later unloading stages, because a pore-pressure increase at approximately fixed total stress reduces effective stress and later pressure dissipation may reload the same material [10,16,40–42]. The published unloading moduli of this test, 8.3 GPa for the first unloading and 3.8 GPa for subsequent unloading [65], form the caprock unloading branch of the simulations (Section 2.6); they are not combined with the primary-loading fit.

2.6. Coupled and Site-Model Simulations

Two configurations were run in OPM Flow 2026.10-rc2, built from source [33]. The first is a layered reservoir–caprock–overburden model of the Smeaheia screen, with CO_2–brine flow and dissolution (CO2STORE) coupled to linear poroelastic mechanics discretized by the two-point stress approximation (TPSA) [34,35]. Its grid is graded and face-orthogonal, as TPSA requires: 500 m cells at the well grow by a factor of at most 1.3 to a lateral boundary 118 km from the well, with 10 m layers through the 79 m caprock and the 100 m reservoir (52,675 cells; Figure 3a,b). Depths and pressure gradients follow the Smeaheia well log of the archive [26]; the injection rate of 3.2 Mt CO_2 yr^{-1} for 50 years, reservoir porosity 0.26, permeability 690 mD and $k_v/k_h = 0.1$ follow Rahman et al. [25]. Every input and its status (sourced, calibrated or assumed) is listed in Table A1. The top surface is free, and the other boundaries have zero displacement.

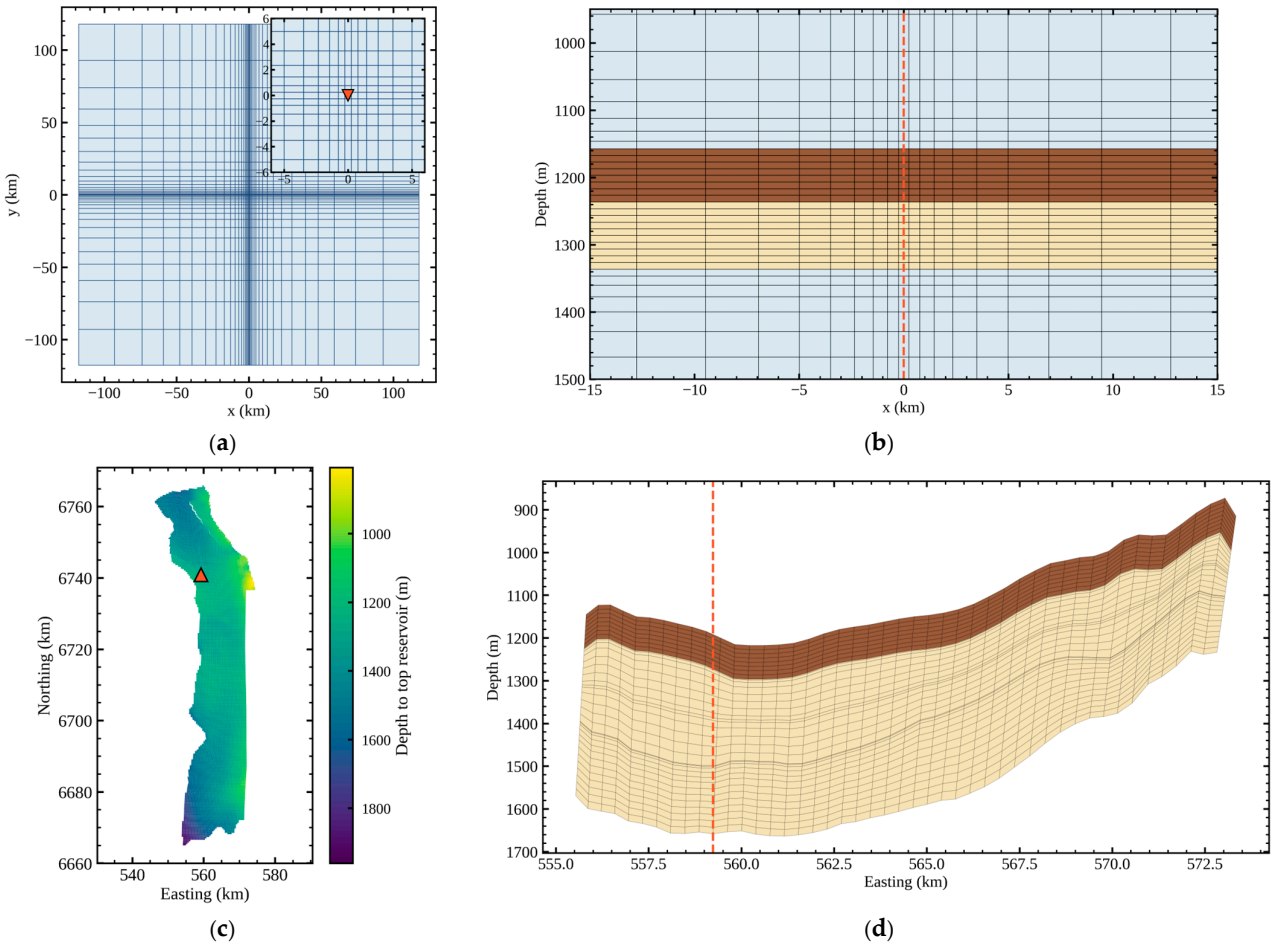


Figure 3. Simulation grids. (**a**,**b**) Layered coupled model: (**a**) plan view, 35 × 35 graded cells, 500 m at the well and growing by at most 1.3 (inset: central ±6 km); (**b**) section through the well: 10 m cells in the caprock (brown) and reservoir (sand), over- and underburden in blue, well dashed. (**c**,**d**) Published Smeaheia model [26] with the added caprock: (**c**) top reservoir layer colored by depth (109 × 253 × 35 cells, 322,280 active; triangle = injector); (**d**) west–east section through the injector row; eight added caprock layers (79 m, brown) over the original layers (sand).

The caprock unloading branch uses the two Draupne unloading moduli, $M_u = 3.8$ and 8.3 GPa [65], as a bound pair, not as a fitted law. In the coupled runs the caprock enters the mechanics through E and ν: the main case uses the drained unloading values measured on vertical sample #7 to 0.1% vertical strain, $E = 4.6$ GPa and $\nu = 0.2$ (loading: $E = 3.7$ GPa, $\nu = 0.14$; Section 4.3.1 of [65]), which gives $M = 5.11$ GPa inside the bound pair; the bounds use $E = 3.42$ and 7.47 GPa at $\nu = 0.2$. In the uncoupled runs the same branch enters as a caprock pore-volume compressibility $c_p = 1/(\varphi_c M_u)$.

The laboratory law reaches the simulator only as tables: (i) Equation (14) is evaluated over the planned stress interval; (ii) Equation (7) is tabulated as pore-volume multipliers against pressure, forming the virgin (loading) curve; and (iii) elastic unloading–reloading curves from the measured modulus are added with ROCKTABH and the HYSTER option (at least two elastic curves), with caprock regions assigned by ROCKNUM. The simulator never evaluates AJOP. A rock-compressibility table must not be combined with poroelastic coupling in the same cells, because both add pore storage; in a test this double counting lowered the reservoir buildup by 30%, so the coupled results use the mechanics alone.

The second configuration is the published Smeaheia pre-feasibility simulation model of Gassnova, released on CO2DataShare (109 × 253 × 27 corner-point cells, 248,616 active; Figure 3c,d) [26]. It ran in OPM Flow without modification. Its single rock compressibility, 4×10^{-5} bar^{-1}, equals the archived reference value, and its schedule injects 1.506 Mt CO_2 yr^{-1} from 2022 to 2047, while brine producers at the southern boundary are set to withdraw 60,000 Sm^3 d^{-1} from 1999 to 2060 (the rate is held until about 2023 and then falls, limited by bottom-hole pressure, to 45–52% of that rate by 2060; the injection runs produce at a higher rate than their twins, about 5% at the end of injection in 2047 and 9–11% by 2060, so the increment includes this producer response); the model does not state what these producers represent. Because the model has no caprock cells, eight layers (79 m in total; porosity 0.1892 from the Draupne specimen; permeability 1×10^{-3} mD, assumed) were stacked on its top surface, and all edits are recorded in File S3. To separate the response to injection from the regional pressure decline, every case was run twice, with the injector open (run A) and shut (run B), and the injection-induced increment $\Delta p_{inj} = p_A - p_B$ was evaluated cell by cell. The end-of-injection value at 1 January 2047 is reported, because later increments also contain an interaction between the gas plume and the continuing depletion. Only flow is simulated on this grid; TPSA is not used on corner-point cells.

A reversal-referenced unloading stiffness of the MIT-S1 type [68] was run only as a secondary illustration: it was fitted to four unloading points from one specimen, one parameter lies at its bound, it is not identifiable, and no conclusion uses it (with it, the Reference case at 51 GSm^3 would fall to 32.0 bar, below the 33 bar screen). Halving the cell size in the fine zone of the layered model (500 to 250 m laterally, 10 to 5 m vertically) changed the reservoir buildup by +0.4%, the caprock pressure by +1.7% and the seabed uplift by −2.0%; moving the lateral boundary from 118 to 196 km changed results by at most 0.04% and doubling the underburden by at most 0.8%. Mass balance closed within 0.21% in the published-model runs. All simulations used a maximum substep of 45.7 days. Halving it to 22.8 days changed the layered-model buildup, caprock pressure and uplift by at most 0.3% and the Reference cases at 51 and 160 GSm^3 of the twelve-case set (constant and 3.8 GPa caprock) by at most 0.1%, with no change of screening class. On the published model it changed the end-of-injection increments by at most 0.9% and moved the caprock-law reductions of Section 3.6 by at most 0.7 percentage points.

Supplementary File S1 contains the source records, fitting protocols, parameters, point-wise predictions, numerical tables and figure scripts of the original analysis; File S2 groups the full-data, blocked, cutoff, interior-holdout and exploratory analyses; and File S3 contains

the simulation inputs, rock tables, edit scripts, re-analysis scripts and outputs. Historical outputs retain their original protocols and are not pooled into a new prediction score.

2.7. Use of Generative AI Tools

During the preparation of this work, the authors used Claude Opus 5.5 (Anthropic) and ChatGPT-6.1 Sol Light (OpenAI) to assist with manuscript editing and language refinement and with drafting simulation input files and scripts for data processing, figure preparation and numerical cross-checking. All scientific content, mathematical formulations, interpretations, and conclusions were developed by the authors, and all calculations and results were reviewed and verified by the authors. The authors subsequently reviewed and edited all AI-assisted content and take full responsibility for the content of the published article.

3. Results

3.1. Representation Across Nineteen Trajectories

Table 2 and Figures 4–9 summarize the representation level. AJOP5 gave a median normalized RMSE of 1.272% (95% CI over trajectories 0.805–1.743%) and a maximum of 3.412%; AJOP4 gave a median of 1.425%, a constant logarithmic slope of 1.726% (maximum 18.88%) and a quadratic of 0.265% (95% CI 0.221–0.372%; maximum 8.807%). In paired Wilcoxon tests across trajectories, AJOP5 did not differ significantly from the quadratic ($p = 0.080$; the quadratic was better in 14 of 19) or from the CF comparator ($p = 0.37$), and it was better than the constant slope ($p = 0.020$). Leave-one-source-out analysis showed that only the result that AJOP5 stays within 5% RMSE holds for every source; the median advantage of the quadratic and the majority of linear-member fits fail on the Hüpers–Kopf records (AJOP5 1.38% against quadratic 2.34% on that source), and all four reversals belong to that source. The maximum pointwise error had a median of 2.50% for AJOP5 (worst 7.64%) and 0.64% for the quadratic (worst 16.7%).

Table 2. Full-window representation across all 19 trajectories. Errors are percentages of each observed void-ratio range.

Model	Median RMSE (%)	Worst RMSE (%)	≤1%	≤2%	≤5%	Monotone Curves
Log-linear	1.73	18.88	5	10	15	19/19
Quadratic	0.26	8.81	15	16	18	15/19
Monotone quadratic	0.26	12.47	15	16	18	19/19
CF power	1.43	4.12	7	12	19	19/19
AJOP4	1.43	3.41	7	14	19	19/19
AJOP5	1.27	3.41	8	14	19	19/19

RMSE levels are descriptive counts only and support no conclusion (Section 2.4). All AJOP fits were positive and monotone inside every window; the quadratic had $\lambda_t < 0$ inside the window in four cases.

In twelve AJOP5 and thirteen AJOP4 fits the curvature term was not supported ($\Delta\lambda$ at its zero bound); this is a reduction within the family, not a failed optimization or proof of zero curvature. In the Reece group, five of six AJOP5 fits were linear, with normalized RMSE of 1.43–3.41%, and the quadratic followed the gentle concave-up shape more closely (Figures 4 and 5). The natural incremental-loading curves contain clearer curvature: complete-window AJOP5 normalized RMSE was 1.38%, 1.74%, 0.80% and 0.99% for P07, P09, P10 and P11, whereas the remolded P08 selected a linear member with 3.16% error (Figures 6 and 7). In the Scott–Reece group all eight AJOP5 fits were below 1.73%, five at the zero-curvature bound (Figures 8 and 9); for P13 the line gives 0.48% and curved AJOP5 0.17%, a difference whose importance depends on the accuracy required rather than on classifying the line as unusable.

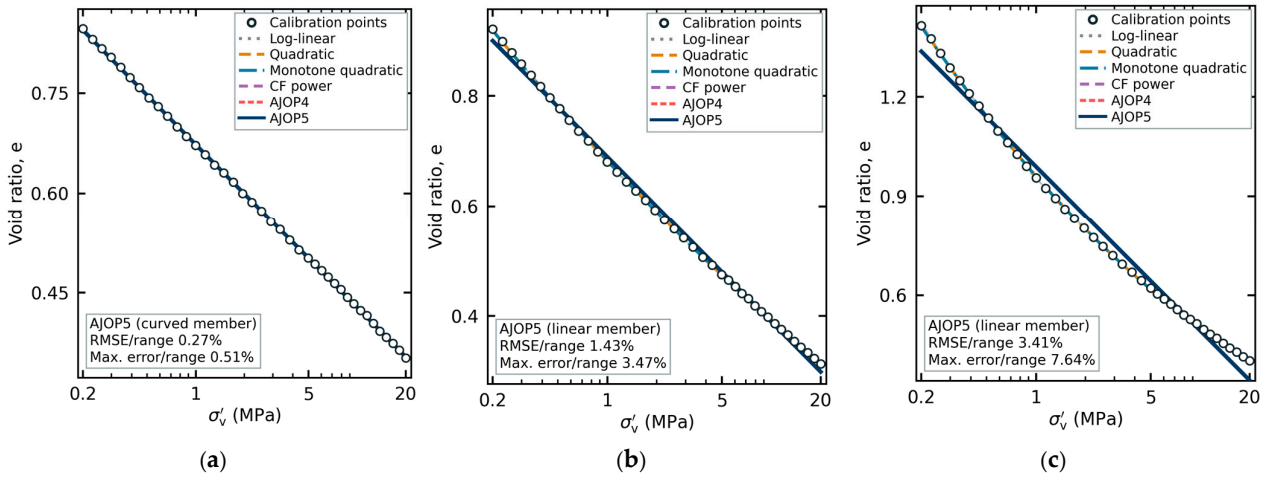


Figure 4. Complete-window calibration of Reece et al. [60] trajectories P01–P03. (**a**) P01, CRS088; (**b**) P02, CRS089; (**c**) P03, CRS090. Symbols are derived calibration locations; pale traces retain the continuous source records. Every model uses every symbol. Curves that coincide can obscure one another. The boxed note in each panel reports AJOP5 errors relative to the observed void-ratio range; these are approximation diagnostics, not independent predictions.

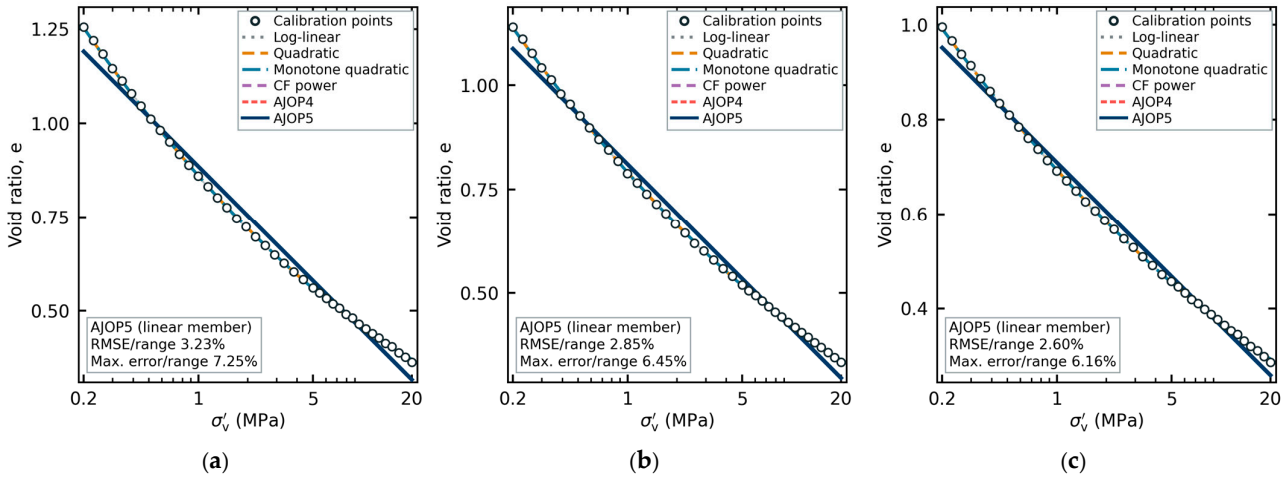


Figure 5. Complete-window calibration of Reece et al. [60] trajectories P04–P06. (**a**) P04, CRS091; (**b**) P05, CRS093; (**c**) P06, CRS094. AJOP4 and AJOP5 reduce to their linear members (curvature term not supported; $\Delta\lambda$ at its zero bound) for all three windows. The quadratic follows the concave-up response more closely. Normalized average and maximum AJOP5 errors quantify the approximation left by the line; symbols, traces, and models follow Figure 4.

The quadratic fitted more closely than AJOP5 in fourteen of nineteen curves, but its largest error was 8.81% against 3.41%, and four quadratic fits (P07, P09, P10 and P11) increased the void ratio with stress inside the window. The monotone quadratic removed these reversals at the cost of a worst normalized RMSE of 12.47%. All AJOP fits were positive and monotone within their windows; positivity at extrapolated stress is examined in Section 3.2.

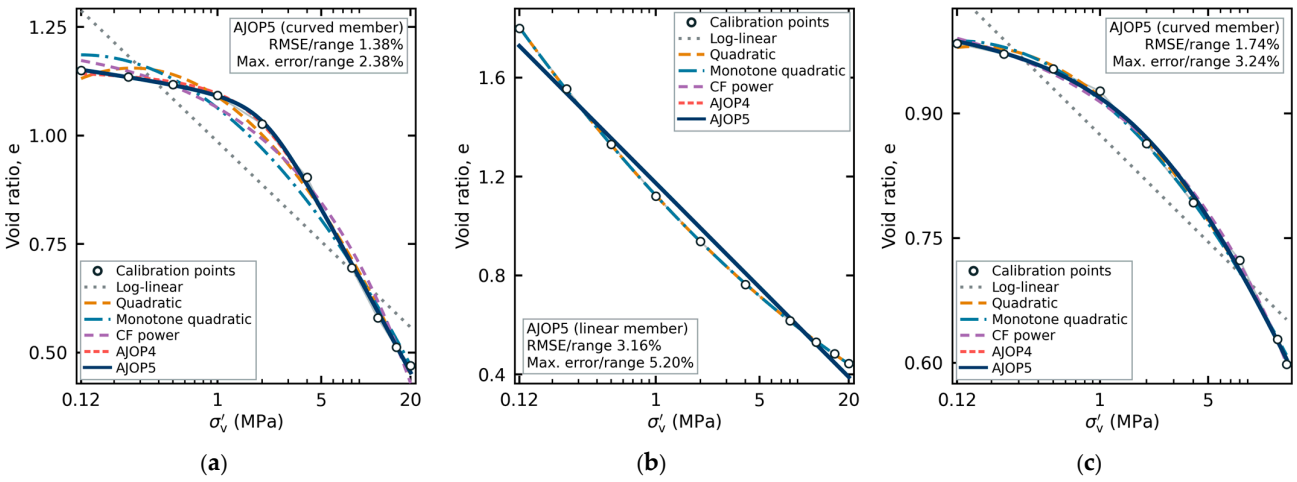


Figure 6. Complete-window calibration of Hüpers–Kopf [61] incremental-loading trajectories P07–P09. (**a**) P07, C0011B-5R-4-85-105; (**b**) P08, C0011B-28R-1-0-17; (**c**) P09, C0011B-35R-5-67-87. P07 and P09 are natural samples; P08 is remolded. Every plotted source endpoint enters calibration. The positive-curvature P08 window selects a linear AJOP member, whereas P07 and P09 require curvature. The residual panels in S2 show small differences between overlapping curves.

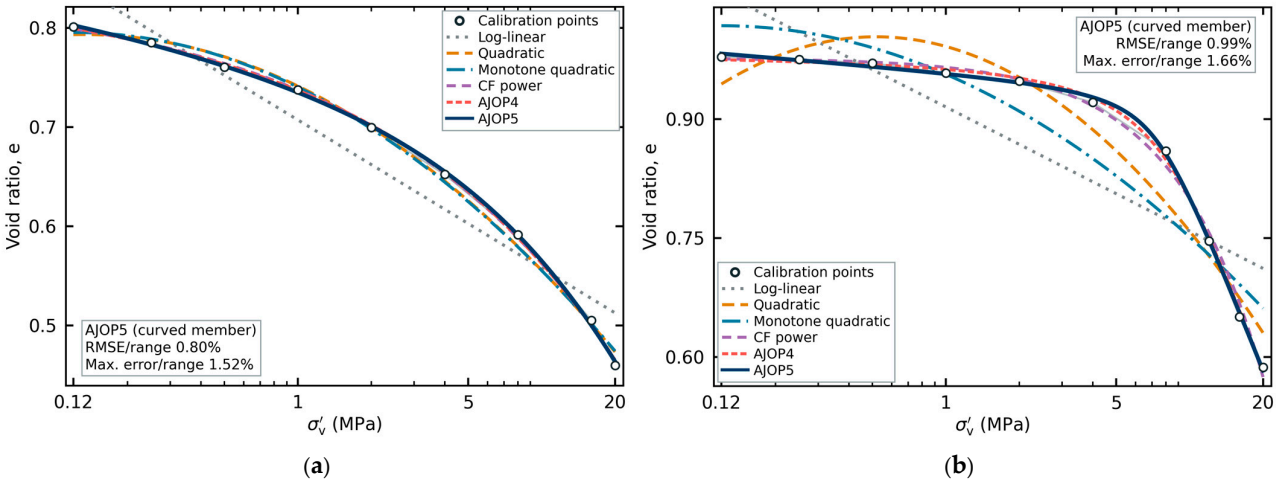


Figure 7. Complete-window calibration of Hüpers–Kopf [61] natural incremental-loading trajectories P10 and P11. (**a**) P10, C0011B-51R-2-48-48; (**b**) P11, C0012A-41R-2-0-18. These cases show the benefit of a transition toward a higher compression slope. Unconstrained quadratic curves reverse direction locally, and enforcing monotonicity increases their residuals. Complete-window fits do not establish prediction from the lower-stress subset.

3.2. Tangent Uncertainty, Identification and Blocked Prediction

A small curve error does not imply a precise tangent property. Propagating the fit residuals by bootstrap (Table 3), the relative half-width of the 95% interval of λ_t was smallest for the Scott–Reece windows and largest for the Hüpers–Kopf incremental-loading records, where it reached 123.4%, and that of c_p reached 152% (P08), although the AJOP5 curve errors of these records were at most 3.16%.

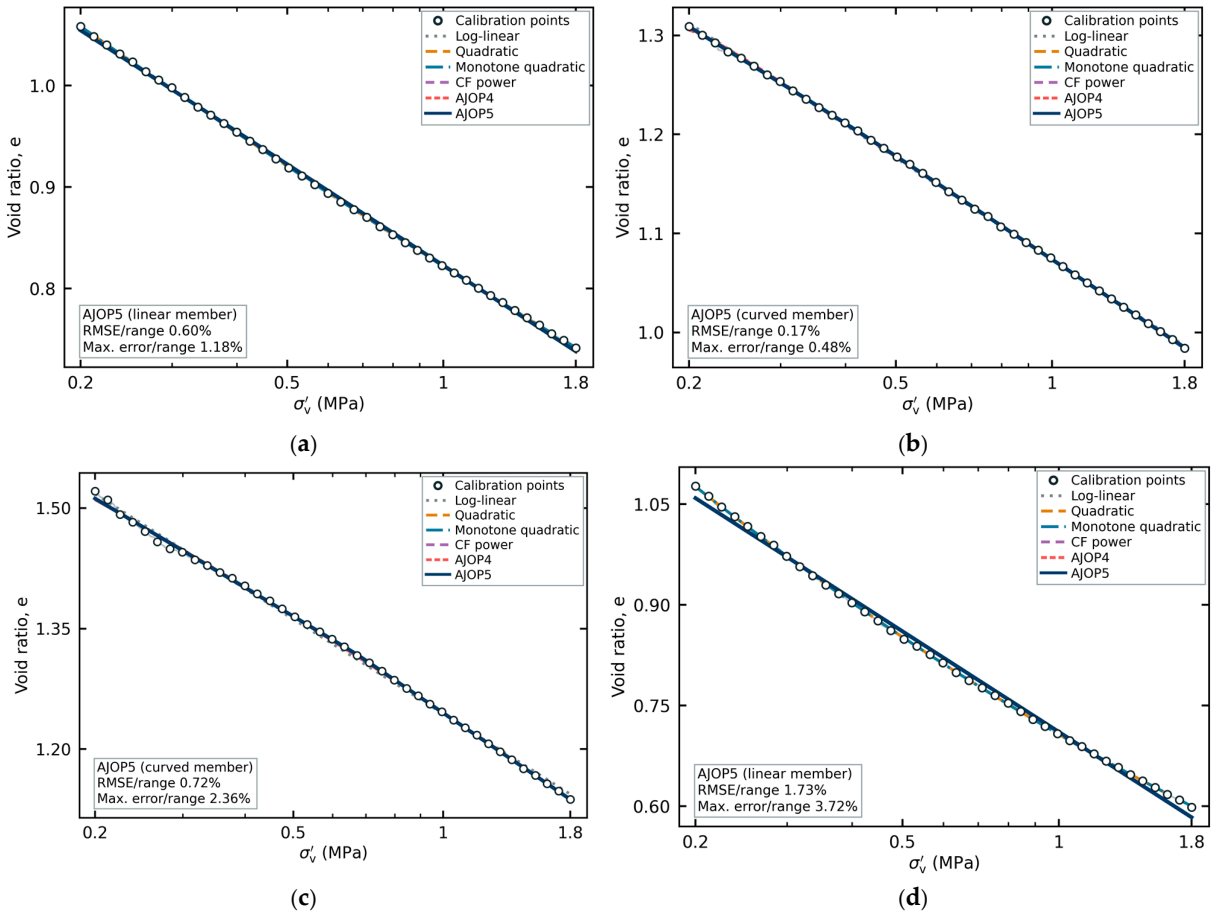


Figure 8. Complete-window calibration of Scott–Reece [62,63] trajectories P12–P15. (**a**) P12, BBC; (**b**) P13, BBC10MDE; (**c**) P14, BBC20MDE; (**d**) P15, EI. BBC denotes Boston Blue Clay, EI denotes Eugene Island sediment, and MDE denotes marine diatomaceous earth; numerals indicate dry-mass percentage addition. P12 and P15 select linear AJOP members, while P13 and P14 retain curvature. All symbols are derived calibration locations.

Table 3. Bootstrap uncertainty of the tangent slope λ_t: relative half-width of the 95% interval inside the observed window ($B = 1000$ per trajectory).

Source (Trajectories)	Median Half-Width	Maximum Half-Width	Grid Share Above 10%
Scott–Reece [62,63] (P12–P19)	0.6–6.7%	2.5–13.6%	0–29%
Reece et al. [60] (P01–P06)	0.9–13.8%	13.1–30.4%	2–100%
Hüpers–Kopf [61] (P07–P11)	6.3–31.8%	21.0–123.4%	24–85%

Ranges are across the trajectories of each source. The largest pore-volume compressibility half-width is 152% (P08). Residual moving-block bootstrap; block length 5 for trajectories with more than 12 points, otherwise 1.

Table 4 summarizes the identification diagnostics. The quadratic or monotone quadratic was AICc-best in 14 of 19 trajectories, nested F tests rejected the constant slope against AJOP5 in 6 of 19, and differential evolution reached the same AJOP5 optimum in every run, so the boundary solutions are properties of the data, not of the optimizer. The two counts answer different questions. The AICc ranks all six forms by in-window misfit penalized for parameter count, whereas each nested F test asks only whether a richer member of one family improves on its simpler member. Curvature in AJOP5 was supported over the constant slope in six trajectories, and the fifth parameter over AJOP4 in only two, consistent with the 12 trajectories whose AJOP5 fit sits at $\Delta\lambda = 0$.

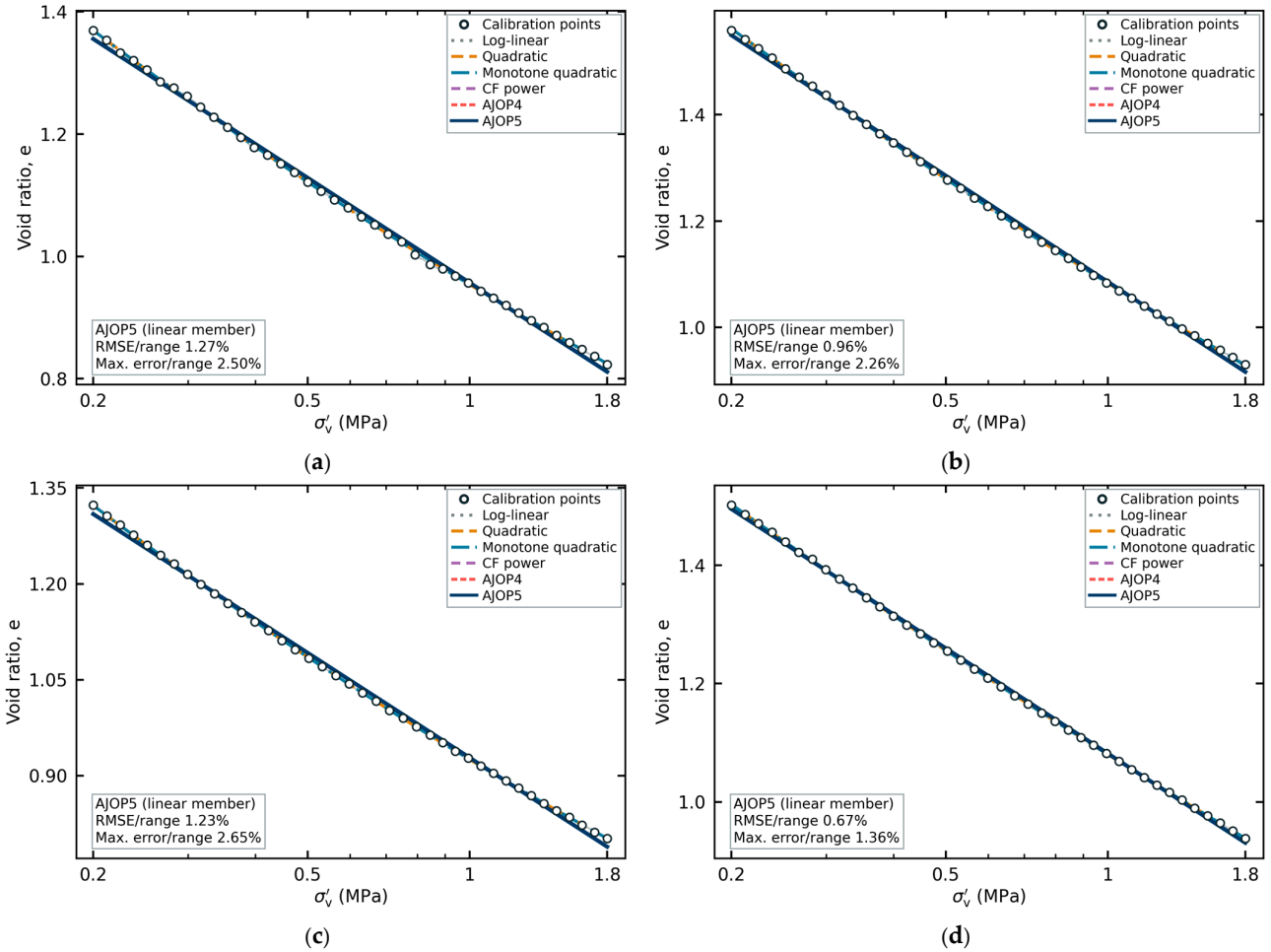


Figure 9. Complete-window calibration of Scott–Reece [62,63] trajectories P16–P19. (**a**) P16, EI10LDE; (**b**) P17, EI20LDE; (**c**) P18, EI10MDE; (**d**) P19, EI20MDE. LDE and MDE denote lacustrine and marine diatomaceous earth, respectively. Each AJOP fit selects the linear member over the observed window. The lower quadratic residuals and the remaining AJOP approximation errors are both retained; none of these curves is an independent field prediction.

Table 4. Information criteria and fit diagnostics across the 19 trajectories.

Diagnostic	Result
AICc-best model (count)	Quadratic 8; monotone quadratic 6; AJOP4 2; AJOP5 2; CF 1
Nested *F* tests rejecting the simpler model	Log slope vs. AJOP5 6/19; log slope vs. AJOP4 6/19; AJOP4 vs. AJOP5 2/19
Boundary hits (AJOP5)	$\Delta\lambda = 0$ in 12 trajectories; θ_c at bound in P01; p_r at bound in P10; $\lambda_0 = 0$ in P09
Multistart convergence (AJOP5)	Differential evolution 4/4 runs in 19/19 trajectories; local starts 97.6% on average, minimum 54% (P01)

Nested tests are nominal; boundary hits indicate lack of data support, not a proven parameter value.

The boundary hits mark where the data stop informing the transition, not where the optimizer failed. Local-start convergence averaged 97.6% but fell to 54% for P01, the only trajectory in which θ_c reached its bound, and differential evolution still returned the same optimum in all four runs. The diagnostics therefore suggest a calibration order: fit the linear member first; retain curvature only when the nested test rejects the line and the transition

parameters lie inside their bounds; and read a lower AICc as a better description of the window, not as a better tangent beyond it, which the blocked predictions below test directly.

The fits also do not extrapolate. Within ten times the maximum observed stress, the fitted laws predicted $e \leq 0$ in nine of 19 trajectories for AJOP5 and AJOP4, 10 for CF, six for the constant slope and one for the quadratic. Tangent properties are therefore reported only inside the observed window, and simulator tables stop there (Section 2.6).

The earlier primary blocked predictions remain materially less favorable to AJOP5: it had lower held-out RMSE than the unconstrained quadratic in three of nineteen cases. The five-case parameter audit concerned only P07, P09, P10, P11, and P13, where the original count was two of five; those denominators must not be interchanged. Extensive searches did not generally remove the prediction errors. Thus, the stronger full-window representation result supports a calibration claim while leaving the adverse prediction evidence intact.

Slope-guided exploratory refits suggest one mechanism without validating a selection rule. For P07, fixing the terminal slope from the last two training endpoints reduced high-stress RMSE from 0.08322 to 0.02090, close to the quadratic value of 0.02041, but the unrestricted AJOP fit performed better in the training-only rolling comparison of model families, so the fixed-slope rule would not have been selected prospectively. File S2 retains these sensitivity plots and the full-data trade-offs.

3.3. Stress Dependence and Prediction in the Draupne Specimen

The six reconstructed primary-loading endpoints of the single specimen are listed in Table 5. The interval logarithmic slope λ_{sec} rose from 0.00453 over 10.98–15.00 MPa to 0.03161 over 50.63–75.96 MPa, a factor of 6.97. In contrast, the log-strain secant constrained modulus varied from 3.50 to 2.39 GPa. The two statements are compatible because Equation (12) contains effective stress and the void ratio: an approximately stable modulus can coexist with a strongly increasing logarithmic slope. This is the central empirical reason not to use the word compressibility without its mathematical definition.

Table 5. Reprocessed Draupne primary-loading endpoints and interval properties; λ_{sec} and M_{sec} refer to the interval ending at each row.

σ'_v (MPa)	e	Interval λ_{sec}	Secant M_{sec} (GPa)
10.98	0.23335	—	—
15.00	0.23194	0.00453	3.50
22.49	0.22865	0.00811	2.81
33.76	0.22408	0.01125	3.02
50.63	0.21647	0.01877	2.71
75.96	0.20365	0.03161	2.39

Endpoints are medians of the final 60 min of each hold. M_{sec} uses logarithmic strain from Equation (4).

Using the first and last observed interval slopes as finite-window extrema gives a diagnostic slope ratio of 6.97 and a minimax relative error of 74.9% for one constant slope over those extrema. This is not an estimate of the asymptotic parameters in Equation (13), because the six endpoints do not demonstrate that either asymptote was reached. It is a direct finite-window result. The ratio remained between 6.96 and 6.97 when the endpoint window changed from 30 to 120 min, so the conclusion is not caused by the one-hour endpoint rule.

The raw chronology confirms that branch choice is not a minor detail. Endpoint secant moduli were 6.14 GPa for the first unloading, 5.83 GPa for reloading, 8.08 GPa for the high-stress unloading step, and 3.27 and 2.64 GPa for the later unloading stages. These values depend on the selected endpoints and are not identical to the tangent moduli reported

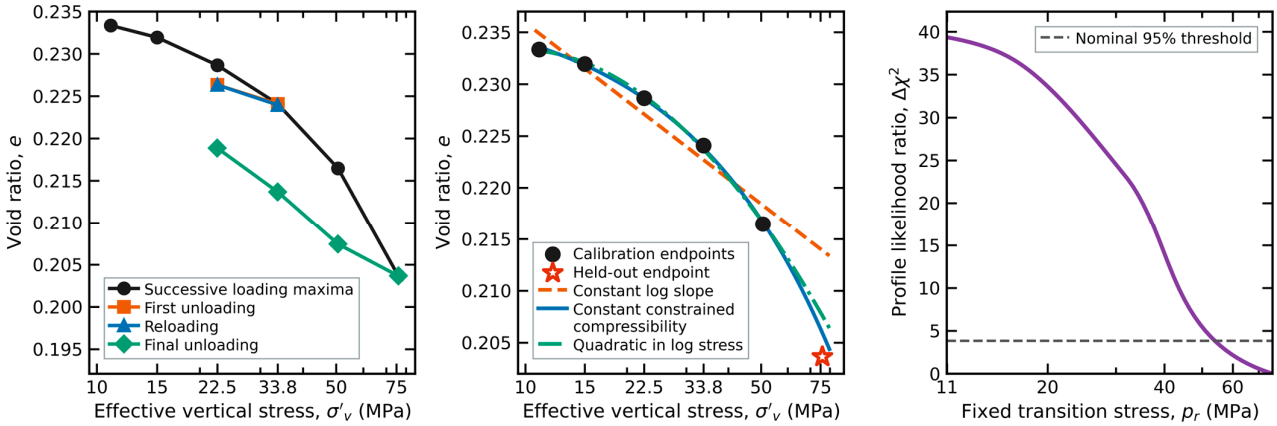
by Soldal et al. [65], but their ordering shows that one primary-loading parameter cannot represent the complete cycle.

The high-stress holdout distinguishes interpolation from prediction (Table 6 and Figure 10). Calibrated through 50.63 MPa, the constant-log-slope model overpredicted the held-out void ratio by 0.01025. This error equals 79.9% of the observed void-ratio change over the held interval. Constant constrained compressibility reduced the error to 0.00230, or 18.0% but still exceeded the 10% constitutive screen; the quadratic error was 0.00396 or 30.9%. Within-specimen leave-one-out cross-validation gave RMSE values of 0.005608, 0.001124, and 0.002072 for these three models, respectively, and therefore preserved the same low-order ranking. These cross-validation values do not estimate between-specimen performance. With the transition-stress bound set only from the five training endpoints, the nested transition gave a holdout error of 0.00211, or 16.4%. It also exceeded the 10% screen and had only one residual degree of freedom, so it remains a diagnostic rather than a validated predictor.

Table 6. Draupne model comparison and 75.96 MPa tail holdout.

Model	p	RMSE e	AIC_c	Holdout $\|\Delta e\|$	Tail Error (%)	Status
Models compared by AICc ($p \leq 3$)						
Constant log slope	2	0.00313	−51.19	0.01025	79.9	Estimable
Constant constrained compressibility	2	0.00053	−72.59	0.00230	18.0	Estimable
Quadratic in log stress	3	0.00068	−39.48	0.00396	30.9	Estimable
Diagnostic only ($p > 3$; AICc undefined for $n = 6$)						
Nested transition	4	0.00010	—	0.00211	16.4	One residual df
Full transition	5	0.00009	—	—	—	Holdout inadmissible
Uyeturk–Germaine	5	0.00013	—	—	—	Holdout inadmissible

Tail error is |prediction − observation| divided by the observed void-ratio change from 50.63 to 75.96 MPa. AIC_c is undefined where $n - K - 1 \leq 0$.



(**a**) (**b**) (**c**)

Figure 10. Reprocessed Draupne oedometer evidence. (**a**) Stable endpoints with loading, unloading, and reloading kept separate. (**b**) High-stress prediction after fitting only the first five primary-loading endpoints; the 75.96 MPa point is held out. (**c**) Profile-likelihood diagnostic for transition stress p_r. The minimum occurs at the upper data boundary, and the nominal 95% set is one-sided. Panel (**c**) is diagnostic because the full fit has one residual degree of freedom.

For the two-parameter models, the all-data constant logarithmic slope was 0.01465 with a nominal 95% t interval of 0.00816–0.02113. The constant constrained compressibility was 3.7389×10^{-4} MPa^{-1}, with an approximate 95% interval of $3.4726\times10^{-4}-4.0053\times10^{-4}$ MPa^{-1}. Expressed per bar, the estimate is 3.74×10^{-5} bar^{-1}, numerically close to the Smeaheia reference value. This numerical proximity does not establish equivalence: constrained compressibility and reservoir pore-volume compressibility have different definitions and stress-path assumptions.

Among the models with $p \leq 3$, constant constrained compressibility was best by every criterion (AICc −72.59, BIC −85.22, RMSE 0.00053, leave-one-out RMSE 0.0011).

The unrestricted five-parameter fits had smaller in-sample RMSE, but the information needed to interpret them was absent. The AIC_c is undefined for both five-parameter models at $n = 6$ when residual variance is counted. A five-point calibration contains no residual degrees of freedom for a five-parameter holdout, so no tail prediction is reported. For the transition law, the scaled-sensitivity condition number was 1.22×10^3, the optimum p_r was 75.96 MPa at the imposed upper boundary, and the nominal profile set extended from 54.19 MPa to that boundary. The profile therefore has no interior upper limit. The Uyeturk–Germaine fit had a scaled condition number of 1.71×10^7. These diagnostics reject physical interpretation of either five-parameter fit from this specimen alone, even though both interpolate the six endpoints closely. For AJOP5, the weakest scaled-sensitivity direction combines e_r (+0.75), $\Delta\lambda$ (−0.52) and ln p_r (−0.39); in the Uyeturk–Germaine fit, e_t and ln e_z cancel (−0.68 each). No parameter of either five-parameter fit is interpreted physically.

3.4. Independent RBBC Specimens Before and After Exclusion

The RBBC cohort addresses variation between independently prepared specimens. Across the cohort of 13 specimen endpoints, the quadratic gave the smallest AICc (−88.25) and LOSO RMSE (0.02901). Uyeturk–Germaine gave a lower full-data RMSE of 0.01980, but its scaled-sensitivity condition number was 5.72×10^8, preventing a physical interpretation of its fitted parameters. AJOP reduced to its linear member ($\Delta\lambda$ at its zero bound) and returned the same full-data RMSE of 0.02988 as the log-linear relation. This is a valid reduced approximation within the AJOP family; the full cohort does not identify additional transition structure.

Under the pre-declared screening rule (Section 2.5), the AICc order was unchanged, with the quadratic best, but the leave-one-specimen-out ranking changed: Uyeturk–Germaine (0.0282) moved ahead of the quadratic (0.0298). In the screened cohort Uyeturk–Germaine identifies only the product $r{\cdot}m$ (scaled condition number 9.87×10^8), and AJOP again reduced to its linear member (Table 7). Figure 11 shows the primary-cohort fits and blocked predictions.

The Uyeturk–Germaine relation had the smallest high-stress RMSE, 0.04939, followed by a constant logarithmic slope at 0.06069 and the quadratic at 0.07708. Constant constrained compressibility gave 0.81911. The monotone transition fit reached the $\Delta\lambda$ and θ_c bounds in the calibration cohort and produced nonphysical extrapolation, with RMSE 1.70066. The Uyeturk–Germaine relation remained the lowest-error high-stress predictor in the strict-K and inclusive cohorts, with RMSE values of 0.03601 and 0.01452, respectively; its condition number nevertheless prevents physical parameter interpretation. Excluding TX1030 in the additional source-audit sensitivity changed the blocked-test ranking: the constant logarithmic slope and collapsed transition law gave RMSE 0.04867, compared with 0.08243 for Uyeturk–Germaine and 0.13714 for the quadratic. The quadratic still minimized the AICc. Thus, the primary-cohort holdout advantage of Uyeturk–Germaine is not robust to this exclusion. Independent specimens make the five-parameter holdout admissible, but admissibility does not establish robust prediction or physically interpretable parameters.

The framework therefore prevents an attractive in-sample fit or parameterization from being transferred as constitutive evidence when the required prediction and identification tests do not support it.

Table 7. Independent-specimen RBBC model comparison and blocked high-stress prediction.

Model	p	LOSO RMSE e	High-Stress RMSE e	Full RMSE e	AIC_c	Diagnostic
Primary cohort (13 specimens; calibration $n = 10$, test $n = 3$)						
Constant log slope	2	0.03885	0.06069	0.02988	−82.61	Estimable
Constant m_v	2	0.25783	0.81911	0.16871	−37.60	Poor prediction
Quadratic log	3	0.02901	0.07708	0.02036	−88.25	Best AIC_c and LOSO
Monotone transition	5	0.03885	1.70066	0.02988	—	Boundary-limited
Uyeturk–Germaine	5	0.03051	0.04939	0.01980	−75.98	Ill-conditioned
Screened cohort (10 specimens; pre-declared rule, Section 3.5; calibration $n = 7$, test $n = 3$)						
Constant log slope	2	0.03895	0.05834	0.02832	−61.28	Estimable
Constant m_v	2	0.27168	0.83975	0.17075	−25.35	Poor prediction
Quadratic log	3	0.02975	0.13341	0.01771	−64.67	Best AICc
Monotone transition	5	0.03895	0.05834	0.02832	—	Linear member ($\Delta\lambda = 0$); ties log slope
Uyeturk–Germaine	5	0.02822	0.21198	0.01679	−41.74	Best LOSO; ill-conditioned (9.87×10^8)

Primary cohort: 13 independent normally consolidated RBBC specimens; calibration $n = 10$ at $\sigma'_v \leq 10$ MPa and test $n = 3$ at $\sigma'_v > 10$ MPa. The AIC_c counts the residual variance as a parameter. The AIC_c entry is suppressed for the singular transition fit; S1 retains its nominal score for transparency. LOSO denotes leave-one-specimen-out, with each fold initialized from its training data only. The transition-law training fit reached the $\Delta\lambda$ and θ_c bounds and extrapolated outside the physical void-ratio range. Screened cohort: TX1030, TX1124 and TX1147 removed under the pre-declared rule (Section 2.5); its Uyeturk–Germaine fit has a scaled condition number of 9.87×10^8, and the monotone transition reduces to its linear member.

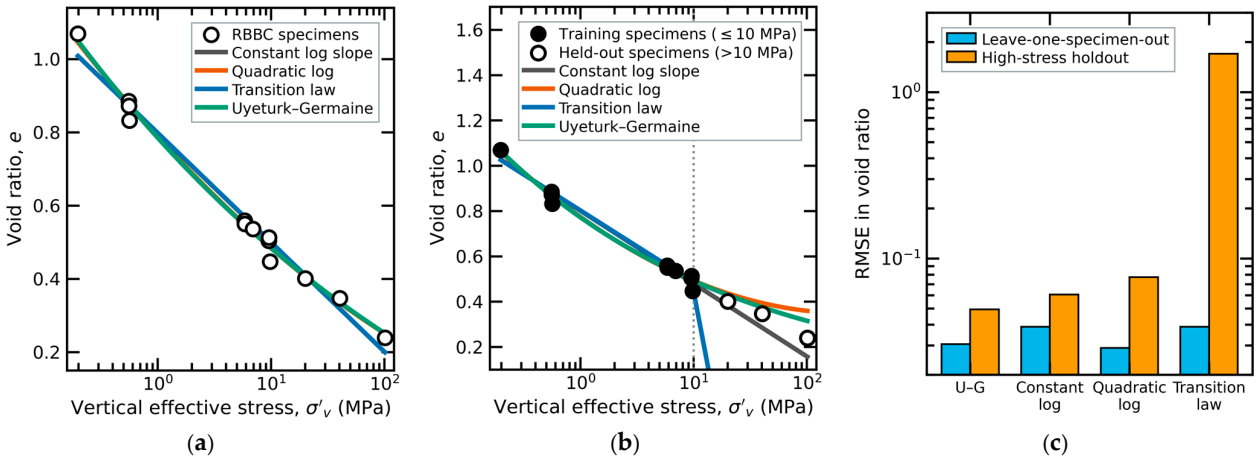


Figure 11. Independent-specimen RBBC stress test using source-tabulated pre-shear consolidation endpoints. (**a**) Primary cohort and full-data fits; the monotone transition law collapses to the constant logarithmic slope. (**b**) Predictions above 10 MPa after calibration on 10 specimens at or below 10 MPa; the transition-law prediction leaves the physical plotting range; its divergence beyond 10 MPa is extrapolation outside the fit window. Constant constrained compressibility is omitted from the panels because of its larger scale but is reported in Table 7. (**c**) Leave-one-specimen-out and blocked high-stress RMSE on a logarithmic axis. (Primary cohort; screened cohort in Table 7).

In the screened cohort the high-stress holdout ranking reversed: constant slope = AJOP (0.0583) < quadratic (0.1334) < Uyeturk–Germaine (0.2120). The large primary-cohort AJOP error arises because its training fit predicts negative void ratios (−0.35, −1.15 and −2.19 at 20, 41 and 101 MPa). No conclusion about model superiority at high stress is drawn from three test specimens.

3.5. Archived Smeaheia Screen and Coupled Layered Model

Table 8 reconstructs the twelve pressure outcomes in the official Smeaheia report [26,27]. Pressure buildup increased as pore-volume compressibility and connected volume decreased. Across all twelve compressibility–volume combinations, four exceeded the 33 bar pre-fractured-caprock screen and two exceeded the 65 bar intact-caprock screen. Both 65 bar exceedances occurred for the low connected-volume case. For the base connected volume of 160 GSm^3, the three compressibility assumptions produced 39, 25, and 15 bar after 50 years. The archived property choice therefore spans 24 bar within that geological model, injection case, and connected-volume assumption.

Table 8. Archived Smeaheia pressure buildup after 50 years of 3.2 Mt yr^{-1} injection [26,27].

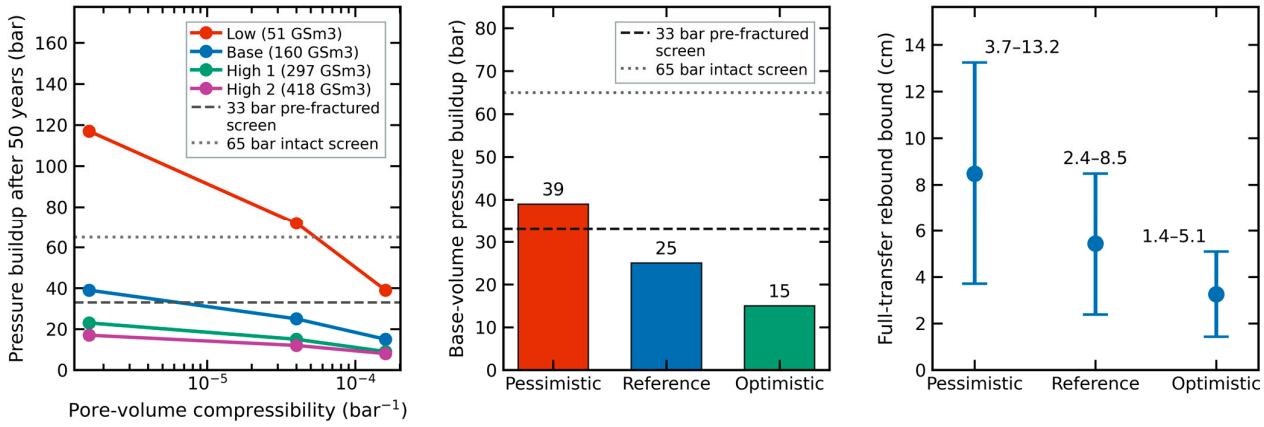
c_p (bar^{-1})	Low 51 GSm^3	Base 160 GSm^3	High 1 297 GSm^3	High 2 418 GSm^3
1.6×10^{-6}	117	39	23	17
4.0×10^{-5}	72	25	15	12
1.6×10^{-4}	39	15	9	8

Values are pressure buildup in bar. The original report scaled the base simulation to alternative connected volumes.

For the base connected volume, reclassification against the updated integrity screens changes the engineering conclusion. The 39 bar case exceeds the conservative 33 bar pre-fractured-caprock screen by 6 bar, whereas the 25 and 15 bar cases remain below it by 8 and 18 bar. All three remain below the 65 bar intact-caprock screen by 26–50 bar. Across the full twelve-case archive, classification depends jointly on pore-volume compressibility and connected volume; the exercise does not identify which input is correct. It does show that the documented property range is large enough to alter a project-specific screening outcome.

Figure 12 shows the archived pressures against both screens. A first-order caprock rebound under full pressure transmission ($T = 1$) is given in Appendix B as an end member of the deformation scale (Figure 12c; Table A2); deformation is evaluated with the coupled model below.

In the coupled layered model (Figure 3a,b; Table 9), the 50-year reservoir buildup of the reference case was 10.97 bar with M_u = 3.8 GPa and 11.62 bar with 8.3 GPa (11.24 bar in the main case). Pore pressure rose by 0.05–0.11 MPa near the caprock top and by 1.60–1.68 MPa near its base, while the vertical total stress changed by only about 0.01 MPa, so the vertical effective stress fell by almost the full pore-pressure rise ($\Delta\sigma'_v = -1.59$ to -1.67 MPa near the base). In this hydrostatic, injection-only setting the caprock is therefore on its unloading branch over its full thickness, and the measured unloading moduli, not the loading envelope, control caprock storage. Seabed uplift was 2.27–2.68 cm, about one-tenth of the 26 cm reported by Rahman et al. [25]. The difference is not a domain effect and is not resolved here: their imposed pressure was 2.2 times ours, and our reservoir thickness and moduli are assumed (Table A1).



(**a**) (**b**) (**c**)

Figure 12. Smeaheia archival pressure and screening consequences. (**a**) Pressure buildup reported for three constant pore-volume compressibilities and four connected-volume cases. (**b**) Base-volume cases compared with the updated 33 bar pre-fractured and 65 bar intact-caprock screens. (**c**) Conditional $T = 1$ rebound range from the 79–129 m thickness and 3.8–8.3 GPa unloading-modulus bounds. Panel (**c**) scales linearly to zero as T decreases and is not a coupled displacement prediction. Panel (**c**) is detailed in Appendix B.

Table 9. Coupled layered model, reference case (160 GSm^3), 50 years at 3.2 Mt CO_2 yr^{-1}.

Caprock Case	Reservoir Δp (bar)	Caprock Δp (bar)	Δp Near Caprock Top/Middle/Base (MPa)	$\Delta\sigma'_v$ Near Caprock Base (MPa)	Seabed Uplift (cm)
M_u = 3.8 GPa (bound)	10.97	2.69	0.05/0.41/1.60	−1.59	2.68
E = 4.6 GPa, ν = 0.20 (main)	11.24	3.07	0.07/0.49/1.64	−1.62	2.50
M_u = 8.3 GPa (bound)	11.62	3.66	0.11/0.60/1.68	−1.67	2.27
Main case, 129 m caprock	11.25	1.91	0.00/0.15/1.64	−1.62	2.51

Caprock Δp is the pore-volume-weighted average above the flow box. Effective stress is compression-positive, so negative values denote unloading; the vertical total-stress change in the caprock was about 0.01 MPa. Uplift is reported at the seabed; it differed from the caprock-top uplift by at most 0.05 cm.

Across the twelve archived parameter sets at the sourced rate, replacing the archived constant caprock compressibility with constant compressibilities from the two measured unloading moduli changed the reservoir buildup by −19% to +3% and the caprock pressure rise by −53% to +39% but changed no screening class; the reference case at 51 GSm^3 stayed about 1 bar above the 33 bar screen (34.02 bar at M_u = 3.8 GPa). With the sourced rate the layered model gives 26–54% of the archived pressures and the archived class in eight of 12 cases; with the rate calibrated on the reference case at 160 GSm^3 (2.10 times the sourced rate), all 12 classes are recovered, but magnitudes differ by −46% to +9%. The archive is therefore used for classes only, not for magnitudes. A 129 m caprock changed the reservoir buildup by at most 0.32% with the archived constant compressibility or either measured unloading modulus (0.33% with the main-case modulus, M = 5.11 GPa) and changed no class. With the 129 m caprock, the caprock law changed the reservoir buildup by −19% to +3% and the caprock pressure rise by −59% to +44%, again with no change of class.

In the coupled layered model, the caprock stress path was also checked against strength. Because TPSA returns stress changes only, the in situ state was taken from the Smeaheia stress model distributed with the dataset (vertical stress, minimum horizontal stress and pore pressure gradients; Supplementary File S1), with $\sigma_H = \sigma_h$ and a Biot coefficient of 1. Fifty years of injection lowered the mean effective stress at the caprock base by 0.82–0.85 MPa and the deviator stress by 1.16–1.22 MPa (p' 6.11 → 5.25–5.29 MPa; q 5.87 → 4.65–4.71 MPa), so the stress point moved down and to the left in p'–q space

(Figure 13a). Against the Mohr–Coulomb envelope measured on vertical Draupne samples (c = 7.5 MPa, φ = 18.7° [65]), the utilization τ_{max}/τ_f at the caprock base fell from 0.31 before injection to 0.26 after 50 years, and the uniform pore-pressure rise needed to reach the envelope grew from 20.1 to 20.9 MPa, against an injection-induced rise of 1.6 MPa. The horizontal-sample envelope (c = 8.4 MPa, φ = 19.4°) gives utilizations of 0.23–0.27 through the caprock in the injector column after 50 years (0.29 → 0.23–0.24 at the caprock base), and at the caprock base the three caprock stiffness cases differ by less than 0.005. No cell of the caprock (9800 cells in each run) increased its utilization: the reduction is largest at the caprock base next to the injector (0.05–0.06) and falls below 0.005 beyond 50 km (Figure 13b,c). On this path the caprock moves away from shear failure, so the strength check does not contradict the linear-elastic mechanics used here. The check uses intact-rock strength from a core outside Smeaheia and does not address fault reactivation, tensile fracturing at the injector or the in-situ strength of the Smeaheia caprock.

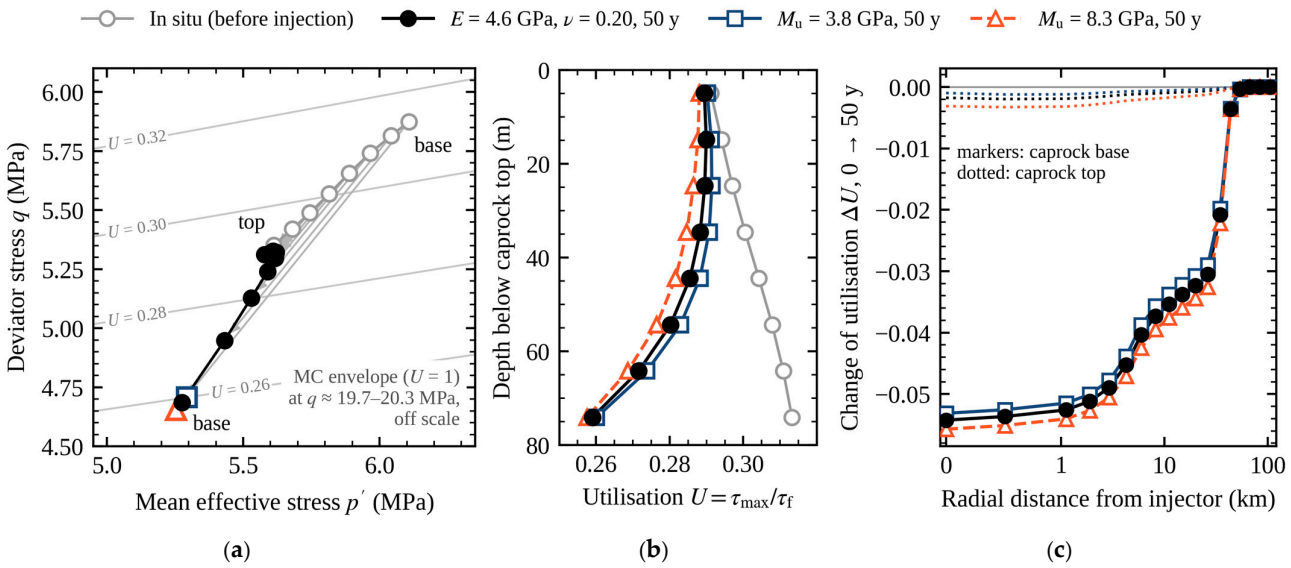


Figure 13. Caprock stress state against intact-rock strength in the coupled layered model (reference case, 160 GSm^3), in situ and after 50 years, for the main case (E = 4.6 GPa, ν = 0.2) and the measured unloading moduli M_u = 3.8 and 8.3 GPa. Utilization $U = \tau_{max}/\tau_f$ refers to the Mohr–Coulomb envelope of vertical Draupne samples (c = 7.5 MPa, φ = 18.7° [65]). (**a**) p'–q states of the eight caprock cells in the injector column; grey lines are iso-utilization lines for axisymmetric states, and the envelope itself (U = 1) lies off scale at $q \approx$ 19.7–20.3 MPa; for the two M_u cases only the caprock base is shown. (**b**) U through the caprock thickness in the injector column. (**c**) Change in U from 0 to 50 years along a radial transect from the injector at the caprock base (markers) and top (dotted lines).

3.6. Published Smeaheia Simulation Model

On the published site model (Figure 3c,d and Figure 14; Table 10), injection raised pressure relative to the no-injection twin by 7.6 bar on average in the reservoir and by 16.5 bar at the top of the injection column at the end of injection (constant c_p), with an increment above 1 bar over about 1440 km^2. The caprock law changed the reservoir increment by less than 4% on average and the increment at the top of the injection column by at most 4.1% but changed the caprock increment substantially: with M_u = 3.8 GPa, the average caprock increment fell from 1.00 to 0.59 bar (−40%) and the maximum at the caprock base from 13.25 to 9.80 bar (−26%; 9.21 bar, −30%, with the HYSTER table) (Figure 15). All these increments are evaluated at the end of injection (1 January 2047) relative to the no-injection twin, and the reductions relative to the constant-c_p run; none of them arises from caprock cells entering the unloading branch. The 3.8 GPa run uses the measured unloading

modulus only to set a single constant caprock compressibility ($c_p = 1.39 \times 10^{-4}$ bar^{-1}) for the whole pressure history, so it tests the stiffness magnitude, not a change of branch. In the HYSTER runs no caprock cell left the loading curve at any restart report before 2047, with or without injection, so the larger reduction comes entirely from the AJOP loading curve, whose compressibility at the in situ state ($1.7–2.2 \times 10^{-4}$ bar^{-1}) exceeds both the archived constant and the 3.8 GPa value. The direction of these effects agrees with the layered model, although there the caprock is on its unloading branch (Section 3.5).

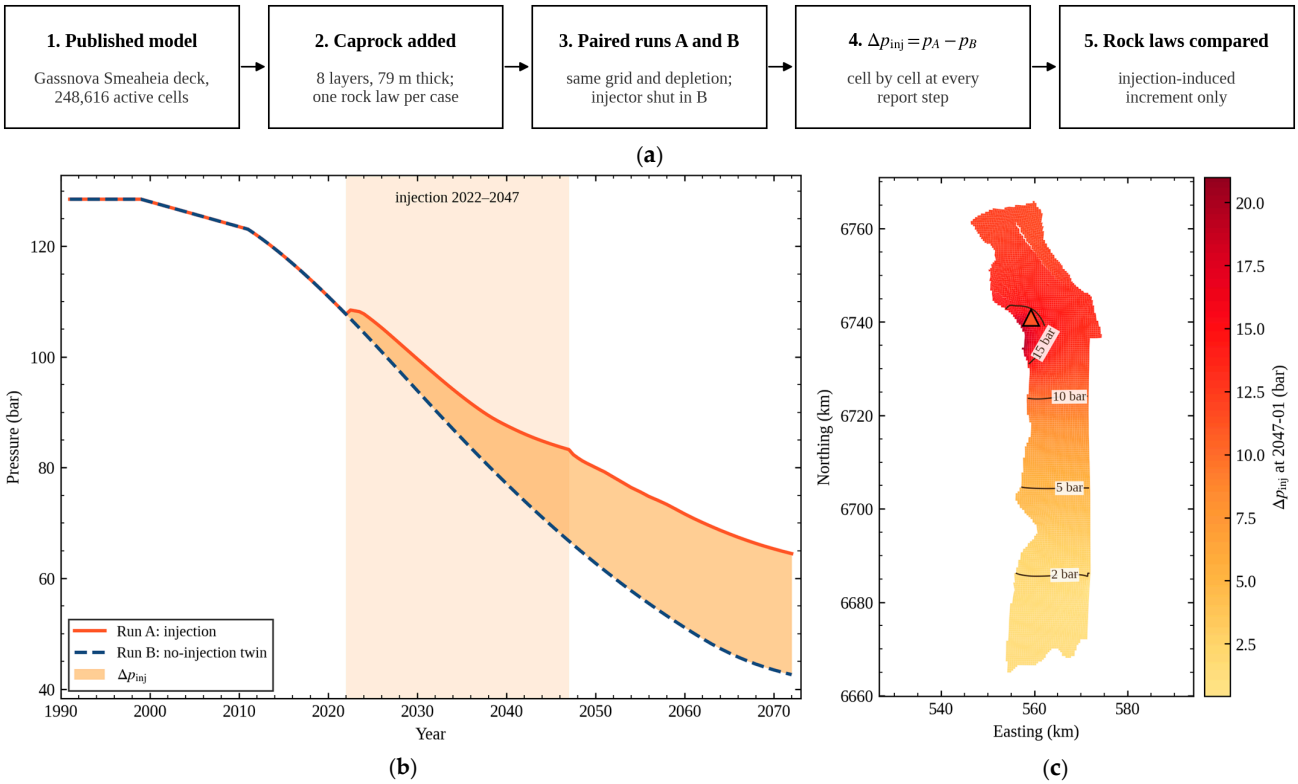


Figure 14. Paired-run evaluation on the published model. (**a**) Workflow: the published model with the documented caprock edits is run with the injector open (run A) and shut (run B), and their difference gives the injection-induced increment Δp_{inj}. (**b**) Pressure at the injector, top reservoir, for constant c_p: the two runs coincide before injection, and the shaded area is Δp_{inj}. (**c**) Δp_{inj} in the top reservoir layer at 1 January 2047, with contours at 2, 5, 10 and 15 bar.

Table 10. Injection-induced increment Δp_{inj} on the published Smeaheia model on 1 January 2047 (run A − run B).

Model/Caprock Law	Reservoir Average (bar)	Top Reservoir, Maximum (bar)	Injector Column, Top Reservoir (bar)	Caprock Base, Maximum (bar)	Caprock Average (bar)
Published model, no caprock	8.28	22.60	17.92	—	—
With caprock, constant c_p	7.64	20.99	16.52	13.25	1.00
With caprock, $M_u = 3.8$ GPa	7.40	20.34	15.97	9.80	0.59
With caprock, HYSTER ($M_u = 3.8$ or 8.3 GPa)	7.35	20.20	15.85	9.21	0.53

Averages are pore-volume-weighted. The two HYSTER cases agree within 0.01 bar to 2060 because no caprock cell leaves the loading curve during injection; the HYSTER row lists the 3.8 GPa case. Percentages in the text are computed from unrounded values.

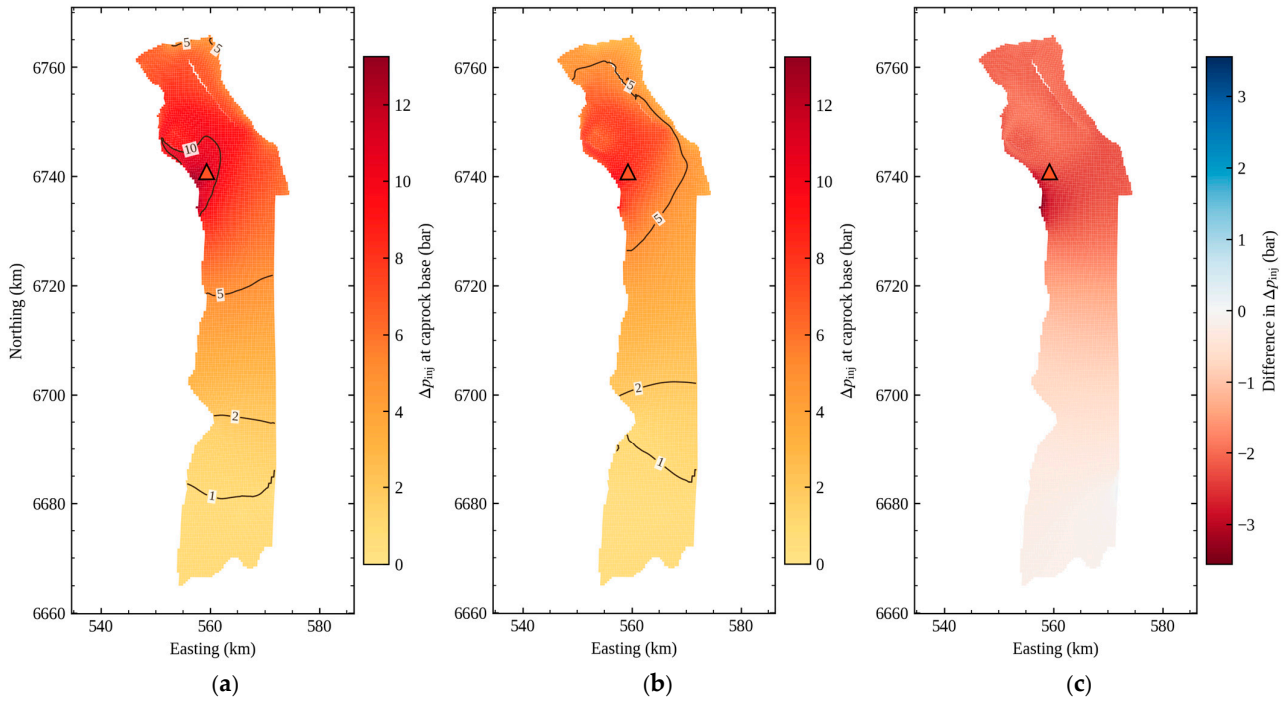


Figure 15. Injection-induced increment at the caprock base, 1 January 2047. (**a**) Constant caprock c_p (archived reference value). (**b**) Measured unloading modulus $M_u = 3.8$ GPa. (**c**) Difference (**b**) − (**a**). Triangle, injector. Contour labels in (**a**,**b**) are in bar.

The stress path differs from the injection-only setting. In the published scenario, regional brine production lowers pressure throughout the injection period: at the injector, the caprock-base pressure fell from 118.5 bar in 2022 to 96.8 bar in 2047 (Figure 16a). In the HYSTER runs no caprock cell left the loading curve during injection (checked at every restart report). Reversals occurred only after the producers stopped in 2060, in 4.6–5.2% of caprock cells and 63–94 bar below their initial pressure, and no reloading occurred before 2072 (Figure 16c). In absolute terms the caprock therefore stayed on loading, and its virgin compressibility governed storage in this scenario.

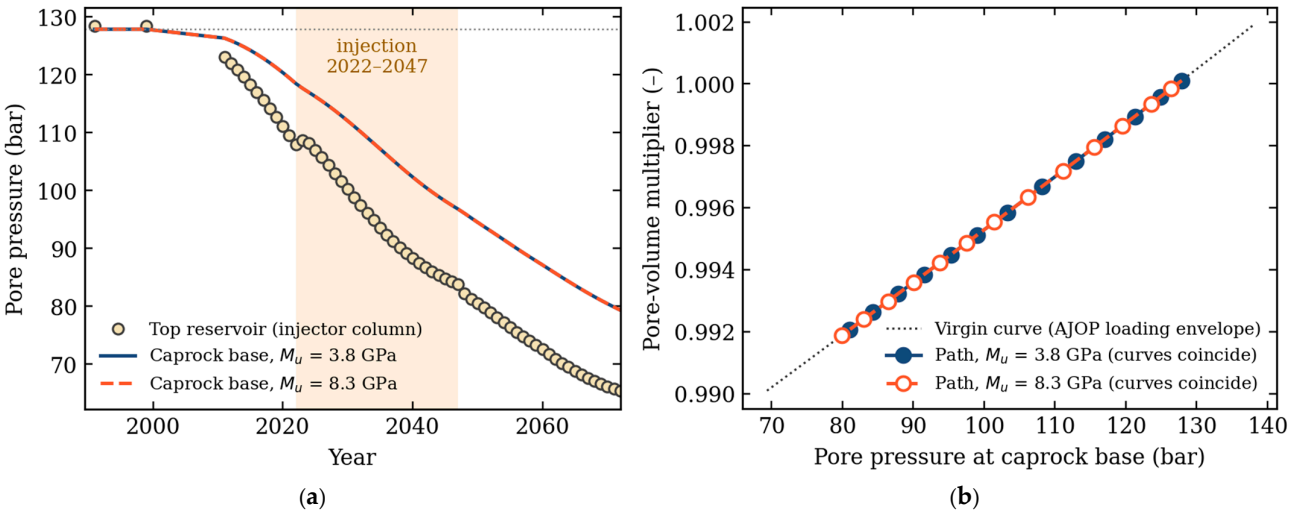
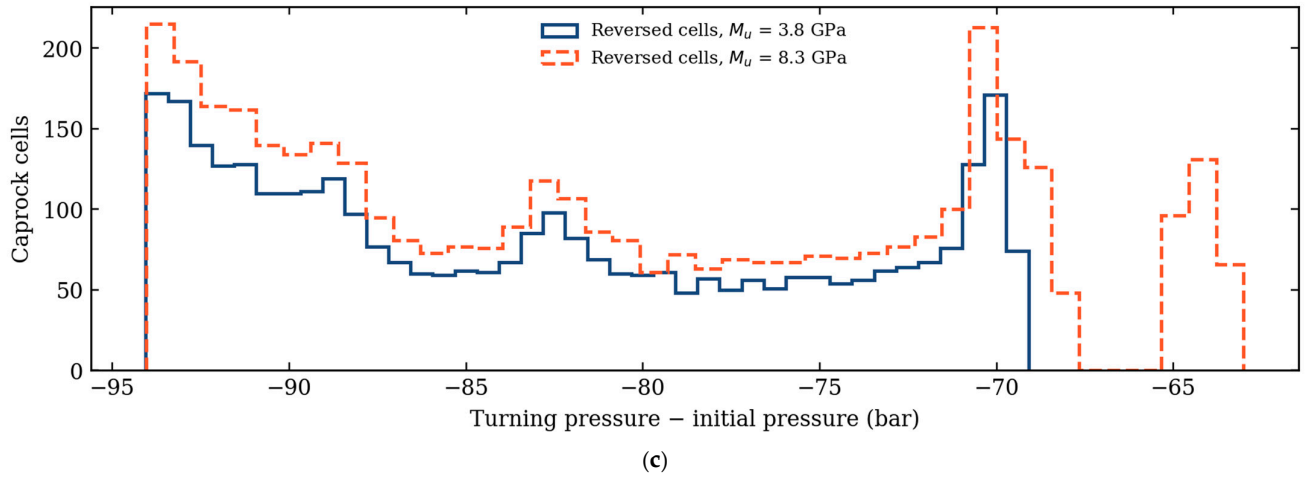


Figure 16. *Cont.*



(**c**)

Figure 16. HYSTER runs on the published model. (**a**) Injector column: pore pressure at the top reservoir (circles) and at the caprock base for M_u = 3.8 GPa (solid) and 8.3 GPa (dashed); the dotted line is the initial caprock-base pressure. (**b**) Caprock-base path in pore-volume-multiplier space: the path stays on the virgin (AJOP loading) curve, so the two moduli give coincident results (markers of the two runs are offset so that both remain visible). (**c**) Caprock cells that reverse, by turning pressure relative to initial pressure: reversals occur only after the brine producers stop in 2060 (4.6% of caprock cells for M_u = 3.8 GPa, 5.2% for 8.3 GPa), and none occurs during injection.

4. Discussion

4.1. What the Laboratory Evidence Supports

The results separate three questions that are often merged. Representation was achievable across all trajectories and survived leaving out each source. Prediction was not: blocked tests favored AJOP5 over the quadratic only in a minority of cases, and neither the Draupne holdout nor the RBBC test supports a transferable transition law. Identification was weakest: the curvature term was unsupported in most fits, the five-parameter Draupne fits were not identifiable, and the RBBC rankings changed under the pre-declared exclusion. A ranking by curve error therefore says little about the tangent property a simulator needs.

Model complexity should follow the information in the calibration window. A nearly straight window supports a reduced linear AJOP member but not a transition location, because it may represent a low-stress branch, a high-stress branch or a narrow part of a smooth curve. A window that begins in a transition needs observations extending far enough to resolve the subsequent branch; additional points within the same early segment cannot constrain the terminal slope. Simplification is adequate where it is tested: Akai et al. [70] found that a simple storage-capacity estimate agreed closely with reservoir simulations under selected conditions, while irreversible compaction limited its accuracy elsewhere, and Lee et al. [36] obtained a nearly linear relation between vertical strain and pore-pressure increase at greater depth despite stronger nonlinearity at shallower depth. These are calibration principles, not a prospectively validated selection rule, and the minimax bound complements them only as an exclusion test: passing it does not validate a reservoir compressibility.

The positive-curvature trajectories show the limit of the AJOP form. AJOP approximates them with its linear member, while a quadratic follows their curvature more closely. Reece et al. report stress-dependent changes in the compression index associated with sediment composition [60], and Scott and Reece document composition and diatom effects [62]; these observations do not support attributing all concave-up behavior to creep. Time, strain rate, fabric, stress history and preparation can affect compression [30,40–51,53], but static

fits cannot separate those mechanisms; a creep explanation would require hold-time or rate-dependent evidence and a time-dependent analysis.

4.2. Loading Envelope, Unloading Branch and the Caprock Path

Within the single Draupne specimen, a strongly increasing logarithmic slope coexisted with a nearly stable secant modulus, and the unloading and reloading moduli differed again (Section 3.3). A compressibility is therefore meaningful only with its definition and its branch, and a loading envelope, however well fitted, says nothing about the stiffness of the branch that injection follows.

Which branch controls the caprock depends on the scenario. In the hydrostatic, injection-only layered model the caprock unloaded over its full thickness and its stress path moved away from the strength envelope, whereas in the published Smeaheia scenario regional brine production kept every caprock cell on its loading curve during injection, so injection unloaded the caprock only relative to the no-injection path. Whether injection unloads a caprock is therefore a site- and scenario-specific outcome, not a general property of CO_2 storage. What the two settings share is the asymmetry of the consequence: the caprock law changed the caprock pressure far more than the reservoir pressure (Sections 3.5 and 3.6), so a reservoir-pressure screen alone is insensitive to the caprock branch that governs caprock storage.

4.3. Consequences for Storage Screening

Whether the remaining property uncertainty matters depends on the decision. Compressibility was not among the five most influential inputs to storage-efficiency uncertainty in the Smeaheia analysis of Wang et al. [28], whereas in the archive the assigned constant alone moved the base-volume case across the 33 bar screen (Section 3.5). These outputs differ, so the reclassification does not establish a universal sensitivity ranking; it identifies a case in which better-supported compressibility inputs could change screening confidence. Demonstrating improved pressure prediction from AJOP would require site-specific branch calibration and a coupled reservoir comparison.

The practical result is an assessment sequence: specify the property, stress window and loading path; quantify approximation and tangent errors; test prediction separately; tabulate a fitted law only inside its observed window; and carry the unresolved property range, including the unloading branch, into the storage screen.

4.4. Limitations

Evidence base. The 19-trajectory analysis is an exploratory benchmark assembled from three published sources that were not sampled to represent storage rocks. Fourteen trajectories are resampled from continuous records and five contain incremental-loading endpoints; their point counts do not measure independent replication, the frozen evaluation locations are unevenly spaced, and the reported counts describe this benchmark, not a probability of success for a new material. Fourteen trajectories are resedimented mixtures and five are ocean-drilling sediments, so the results test the form of compression laws, not intact caprock behavior. No independent trajectory set outside the three sources was available; leave-one-source-out analysis is the nearest substitute.

Single specimen and cohort. All Draupne results, including the unloading moduli used in the simulations, come from one specimen cored outside Smeaheia (Section 2.5). They are not transferable to Draupne shale in general or to the Smeaheia caprock, and the stress range of the measured unloading branch lies above the 6–10 MPa effective-stress range of the Smeaheia screen. Six loading endpoints cannot identify a transferable transition law, and observed finite-window slopes do not prove that an asymptote has been reached. The

RBBC cohort consists of terminal states of different specimens, and its high-stress rankings rest on three test specimens.

Time dependence. The records have no common effective strain rate, and the 30, 60 and 120 min endpoint-window check tests processing stability, not creep. Secondary compression of mudrocks over 1–100 MPa is documented [51] but is not represented in any model here; over 50 years, creep would add compaction at constant effective stress.

Archive and screens. The Smeaheia pressures in Table 8 are archived outputs of constant-compressibility runs, so they show sensitivity to the chosen constant, not superiority of a stress-dependent law. The 33 and 65 bar values are project-report screening limits at the stated reference depth, not general regulatory thresholds, and comparing reservoir-pressure increments with them does not resolve the caprock pressure or stress field. Neither simulation reproduces the 2012 archive, whose injection rate, boundary conditions and pressure definition are not documented.

Simulation scope. The simulations are sensitivity checks, not site predictions. The mechanics are linear elastic, so the caprock unloading branch enters only as a constant modulus, and the HYSTER curves are symmetric between unloading and reloading, with no memory of more than one reversal. TPSA was used only on the face-orthogonal layered grid; on the corner-point published model only flow was simulated, so the coupled model resolves vertical caprock profiles but not lateral structure, which comes only from the flow-only published model. Reservoir thickness, the moduli outside the caprock and the caprock and overburden permeabilities are assumed (Table A1); capillary entry of CO_2 into the caprock is not modeled; the layered model is a closed box without faults; and the published model extrapolates gas properties above 55.9 bar and carries an added caprock of assumed permeability.

5. Conclusions

A constant compressibility assumption should be judged by the engineering output it feeds, and that judgement requires separate checks of curve representation, prediction, parameter identification and consequence. The exact minimax bound identifies primary-loading intervals on which no constant logarithmic slope can meet a stated tolerance; it does not apply to unloading or reloading, which require a separately measured branch. Across 19 published laboratory trajectories, mostly resedimented, AJOP5 stayed within 5% range-normalized RMSE in every trajectory (median 1.27%, 95% CI 0.81–1.74%), yet the curvature term was unsupported in 12 fits, tangent-slope uncertainty reached 123%, blocked predictions were less favorable than full-window fits, and independent-specimen rankings reversed under a pre-declared exclusion, so a small curve error does not certify a tangent property. Fitted laws should therefore be tabulated only inside their observed window and calibrated on data that constrain the branch to be predicted. In flow and coupled sensitivity checks on the layered model with the two measured Draupne unloading moduli, the caprock law changed caprock pressure by up to 59% but reservoir buildup by at most 19% and no screening class, while on the published Smeaheia model the caprock stayed on its loading path during injection. Whether injection unloads a caprock, and therefore which measured branch controls caprock storage, is a site- and scenario-specific outcome that must be established before a compressibility table is used.

Supplementary Materials: The following supporting information can be downloaded at https://www.mdpi.com/article/10.3390/en19215354/s1, File S1 contains the v20 reproducibility package, complete numerical tables, editable figure sources, earlier frozen analyses, verification scripts, source register, and SHA-256 manifest. File S2 contains all 127 analysis figures grouped by purpose and provenance, with full-data calibration separated from prediction and exploratory refits. File S3 contains the layered-model OPM Flow decks, rock tables, the edit scripts for the published Smeaheia

model (the licensed model must be downloaded from CO2DataShare), deck-edit and conversion scripts, the Group-B re-analysis scripts and outputs, the time-stamped pre-declared exclusion rule, the assumptions record of Section 2.6, and the final simulation runs and their time-step check (folder R2_final_runs).

Author Contributions: Conceptualization, N.K. and T.C.; methodology, N.K. and T.C.; software, N.C., N.K. and T.C.; validation, N.K., A.K. and S.E.-a.; formal analysis, N.K. and T.C.; investigation, N.C., T.C., S.I., A.K. and S.S.; resources, N.C., S.I. and S.S.; data curation, N.C., T.C. and S.I.; writing—original draft preparation, N.K. and T.C.; writing—review and editing, N.K., A.K., S.E.-a. and S.S.; visualization, N.C., N.K. and S.E.-a.; supervision, S.I., A.K., S.E.-a. and S.S.; project administration, N.K.; funding acquisition, N.K. All authors have read and agreed to the published version of the manuscript.

Funding: This research project was financially supported by Mahasarakham University.

Institutional Review Board Statement: Not applicable.

Informed Consent Statement: Not applicable.

Data Availability Statement: The Reece et al. and Hüpers–Kopf source workbooks accompany their IODP reports [60,61]. The Scott–Reece workbook is archived on Zenodo, version 2 [63]. The Casey thesis is available from MIT [64], the Draupne laboratory files from DataverseNO [66], and the Smeaheia packages from CO_2DataShare [26]. Supplementary File S1 contains the extracted analysis records, source URLs and hashes, exact transformations, cohort flags, parameters, predictions, and figure scripts. Copyrighted source papers and the Casey thesis PDF are not redistributed. The Smeaheia pressures remain identified as archived outputs. This paper contains data from the Smeaheia Dataset © Gassnova SF and Equinor ASA, licensed under the Smeaheia Dataset License (https://co2datashare.org/dataset/smeaheia-dataset, accessed on 31 October 2026). The caprock overlay and all modified simulation inputs are the authors' adaptations; Gassnova and Equinor do not endorse this work.

Acknowledgments: The coupled and site-scale simulations were performed with the open-source simulator OPM Flow [33]. Generative AI tools (Claude Opus 5.5, Anthropic; ChatGPT-6.1 Sol Light, OpenAI) were used as described in Section 2.7.

Conflicts of Interest: The authors declare no conflicts of interest.

Abbreviations

The following abbreviations and symbols are used in this manuscript:

Abbreviation/symbol	Definition
AIC, AICc	Akaike information criterion; small-sample corrected AIC [57]
AJOP	Arc Joint via Optimum Parameters compression law [52,53]
AJOP4, AJOP5	Four-parameter AJOP; centered five-parameter AJOP (Equation (7))
BBC, RBBC	Boston Blue Clay; resedimented Boston Blue Clay
BIC	Bayesian (Schwarz) information criterion [69]
CF	Positive-exponent power comparator of Phonchamni et al. [53]
CI	Confidence interval
CO2STORE	OPM Flow option for CO_2–brine storage with dissolution
DE	Differential evolution (global optimizer)
EI	Eugene Island sediment
GSm^3	10^9 standard cubic meters
HYSTER	OPM option with hysteresis: loading curve on increasing effective stress, elastic curve after reversal
IODP, ODP	(Integrated) Ocean Drilling Program
KB	Kelly Bushing
LDE, MDE	Lacustrine and marine diatomaceous earth
LOOCV	Leave-one-out cross-validation
LOSO	Leave-one-specimen-out (RBBC)

MIT-S1	Pestana–Whittle unified model for clays and sands [68]
OPM	Open Porous Media (OPM Flow simulator) [33]
P01–P19	Trajectory identifiers (Section 2.1)
RMSE	Root-mean-square error, normalized by the observed void-ratio range unless stated
ROCKTAB, ROCKTABH	OPM pore-volume multiplier tables without and with hysteresis
TPSA	Two-point stress approximation finite-volume mechanics [34,35]
TVD, TVDmsl	True vertical depth; true vertical depth below mean sea level
U–G	Uyeturk–Germaine compression relation [50]
e, e_r	Void ratio; AJOP reference void ratio
λ_t	Local tangent slope, $-de/d \ln \sigma'_v$
λ_0, λ_∞, $\Delta\lambda$	Initial and limiting AJOP slopes; slope contrast $\lambda_\infty - \lambda_0$
θ_c, p_r	AJOP transition sharpness; transition stress
σ'_v	Vertical effective stress
τ	Relative slope tolerance in Equations (13) and (14)
m_v, c_p	Constrained compressibility; pore-volume compressibility
M, M_u, E, ν	Constrained modulus; unloading constrained modulus; Young's modulus; Poisson's ratio
Δp_{inj}	Injection-induced pressure increment (run A − run B)
n, p, B	Number of points; number of parameters; bootstrap resamples

Appendix A

Table A1. Inputs of the coupled and site-model checks (Section 2.6).

Input	Value	Source	Status
Overburden and pore-pressure gradients; seabed 312 m; KB 24 m	Smeaheia well log	Archive [26] (File S1)	Sourced
Reservoir top/initial pressure	1236.5 m TVDmsl/124.97 bar	Archive [26]; hydrostatic as in [25]	Sourced
Injection rate	3.2 Mt CO_2 yr^{-1}, 50 years	Rahman et al. [25]	Sourced
Calibrated rate (comparison only)	2.10 × sourced rate	Reference case at 160 GSm^3 = 25 bar	Calibrated
Reservoir porosity/permeability/k_v:k_h	0.26/690 mD/0.1	Rahman et al. [25]	Sourced
Reservoir thickness	100 m	—	Assumed
Pore volumes; reservoir c_p sets	51/160/297/418 GSm^3; 1.6×10^{-6}, 4.0×10^{-5}, 1.6×10^{-4} bar^{-1}	Archive [26,27]	Sourced
Caprock thickness	79 m (main), 129 m (variant)	Wells 32/2-1, 32/4-1 [27]	Sourced
Caprock porosity	0.1892	Draupne specimen [65,66]	Sourced
Caprock unloading modulus	M_u = 3.8 and 8.3 GPa	Draupne oedometer [65]	Sourced
Caprock E, ν (TPSA main case)	4.6 GPa, 0.2 (M = 5.11 GPa)	Soldal et al. [65], drained unloading, vertical sample #7 (Section 4.3.1 of [65])	Sourced
Reservoir/over- and underburden E at ν = 0.25	8.01 GPa/13.9 GPa	Equivalent to the archived reference c_p	Assumed

Table A1. *Cont.*

Input	Value	Source	Status
Caprock/overburden permeability	$1 \times 10^{-3}/1 \times 10^{-2}$ mD	—	Assumed
Temperature, salinity, Biot coefficient	40 °C, 0, 1.0	—	Assumed
Mechanical boundaries	Top free; sides and bottom fixed	Model choice (no roller condition in TPSA)	Assumed
Published model: grid, rock compressibility, schedule	$109 \times 253 \times 27$; 4×10^{-5} bar^{-1}; 1.506 Mt yr^{-1} 2022–2047	Gassnova model [26]	Sourced
Added caprock in published model	8 layers, 79 m; $\varphi = 0.1892$; 1×10^{-3} mD	[65]; permeability assumed	Assumed

Appendix B

A one-dimensional end-member was added to show the deformation scale without claiming a coupled field solution. At 1260.5 m TVD/KB (1236.5 m TVDmsl, with a 24 m Kelly Bushing elevation), the archived March 2017 stress model gives overburden and pore-pressure equivalent mud weights of 1.826 and 1.011 specific gravity [26]. Using its native TVD/KB convention gives an initial effective vertical stress of 10.074 MPa when Biot's coefficient is set to one. This is an explicit end-member assumption, not a measured site value of that coefficient. Using the 79 and 129 m well thicknesses reported for 32/2-1 and 32/4-1 as illustrative endpoints [27], together with unloading modulus $M_u = 3.8 - 8.3$ GPa, conditional rebound was calculated to first order as $T\,h\Delta p/M_u$, at fixed total vertical stress and with Biot's coefficient set to one. For another specified coefficient, the effective-stress decrement and this first-order rebound are multiplied by that coefficient. These thickness endpoints are not site-wide minimum and maximum bounds. The transmission factor T lies between zero and one: $T = 0$ denotes no caprock pore-pressure transmission, whereas $T = 1$ applies the full reservoir pressure increment uniformly as an upper end-member. The constrained modulus represents zero lateral strain. The calculation does not resolve spatial pressure gradients, site-scale lateral coupling, thermal stress, faults, or poroelastic total-stress redistribution. This end member is retained for scale only; deformation is evaluated with the coupled model in Section 3.5.

The stress log gives an initial effective vertical stress of 10.074 MPa at 1260.5 m TVD/KB. Under the $T = 1$, unit Biot coefficient and fixed-total-stress end-member, the base-volume pressure rises reduce that value to 6.17, 7.57, and 8.57 MPa for the pessimistic, reference, and optimistic compressibility cases, respectively. Combining the 79–129 m thickness range with $M_u = 3.8 - 8.3$ GPa gives conditional rebound ranges of 3.7–13.2, 2.4–8.5, and 1.4–5.1 cm (Table A2). For any $T < 1$, these values scale linearly toward zero.

Table A2. Base-volume Smeaheia integrity margins and conditional full-transmission rebound bounds.

c_p case	Δp (bar)	σ'_v at T=1 (MPa)	Rebound at T=1 (cm)	Margin to 33 bar	Margin to 65 bar
Pessimistic	39	6.17	3.7–13.2	−6	26
Reference	25	7.57	2.4–8.5	8	40
Optimistic	15	8.57	1.4–5.1	18	50

Positive pressure margin denotes a value below the screen. T is an unknown pressure-transmission factor with $0 \le T \le 1$. The table assumes unit Biot coefficient and fixed total vertical stress; rebound is a first-order constrained estimate.

These rebound bounds are conditional one-dimensional estimates, not site predictions of surface movement or caprock deformation. They show the scale introduced by branch-stiffness choice under a stated transmission assumption. The factor between the two unloading-modulus bounds is 2.18, which exceeds the 10% tangent-property screen, but the unknown transmission factor and three-dimensional stress redistribution prevent a site deformation claim. The pressure-screen reclassification in Section 3.5 is therefore the stronger storage consequence, and the main decision conclusion does not depend on the $T = 1$ rebound end-member.

References

1. IPCC. *Climate Change 2022: Mitigation of Climate Change*; Cambridge University Press: Cambridge, UK, 2022. [CrossRef]
2. Bui, M.; Adjiman, C.S.; Bardow, A.; Anthony, E.J.; Boston, A.; Brown, S.; Fennell, P.S.; Fuss, S.; Galindo, A.; Hackett, L.A.; et al. Carbon capture and storage (CCS): The way forward. *Energy Environ. Sci.* **2018**, *11*, 1062–1176. [CrossRef]
3. Bachu, S. CO_2 storage in geological media: Role, means, status and barriers to deployment. *Prog. Energy Combust. Sci.* **2008**, *34*, 254–273. [CrossRef]
4. Benson, S.M.; Cole, D.R. CO_2 sequestration in deep sedimentary formations. *Elements* **2008**, *4*, 325–331. [CrossRef]
5. Ringrose, P.S.; Meckel, T.A. Maturing global CO_2 storage resources on offshore continental margins to achieve 2DS emissions reductions. *Sci. Rep.* **2019**, *9*, 17944. [CrossRef]
6. Szulczewski, M.L.; MacMinn, C.W.; Herzog, H.J.; Juanes, R. Lifetime of carbon capture and storage as a climate-change mitigation technology. *Proc. Natl. Acad. Sci. USA* **2012**, *109*, 5185–5189. [CrossRef]
7. Biot, M.A. General theory of three-dimensional consolidation. *J. Appl. Phys.* **1941**, *12*, 155–164. [CrossRef]
8. Biot, M.A.; Willis, D.G. The elastic coefficients of the theory of consolidation. *J. Appl. Mech.* **1957**, *24*, 594–601. [CrossRef]
9. Nur, A.; Byerlee, J.D. An exact effective stress law for elastic deformation of rock with fluids. *J. Geophys. Res.* **1971**, *76*, 6414–6419. [CrossRef]
10. Rutqvist, J. The geomechanics of CO_2 storage in deep sedimentary formations. *Geotech. Geol. Eng.* **2012**, *30*, 525–551. [CrossRef]
11. Streit, J.E.; Hillis, R.R. Estimating fault stability and sustainable fluid pressures for underground storage of CO_2 in porous rock. *Energy* **2004**, *29*, 1445–1456. [CrossRef]
12. Hawkes, C.D.; McLellan, P.J.; Bachu, S. Geomechanical factors affecting geological storage of CO_2 in depleted oil and gas reservoirs. *J. Can. Pet. Technol.* **2005**, *44*, 52–61. [CrossRef]
13. Birkholzer, J.T.; Zhou, Q. Basin-scale hydrogeologic impacts of CO_2 storage: Capacity and regulatory implications. *Int. J. Greenh. Gas Control* **2009**, *3*, 745–756. [CrossRef]
14. Rutqvist, J.; Birkholzer, J.T.; Tsang, C.F. Coupled reservoir–geomechanical analysis of the potential for tensile and shear failure associated with CO_2 injection in multilayered reservoir–caprock systems. *Int. J. Rock Mech. Min. Sci.* **2008**, *45*, 132–143. [CrossRef]
15. Rutqvist, J.; Vasco, D.W.; Myer, L. Coupled reservoir–geomechanical analysis of CO_2 injection and ground deformations at In Salah, Algeria. *Int. J. Greenh. Gas Control* **2010**, *4*, 225–230. [CrossRef]
16. Thompson, N.; Andrews, J.S.; Bjørnarå, T.I. Assessing potential thermo-mechanical impacts on caprock due to CO_2 injection—A case study from Northern Lights CCS. *Energies* **2021**, *14*, 5054. [CrossRef]
17. Zheng, X.; Espinoza, D.N. Measurement of unloading pore volume compressibility of Frio sand under uniaxial strain stress path and implications on reservoir pressure management. *Rock Mech. Rock Eng.* **2021**, *54*, 5745–5760. [CrossRef]
18. Vasco, D.W.; Rucci, A.; Ferretti, A.; Novali, F.; Bissell, R.C.; Ringrose, P.S.; Mathieson, A.S.; Wright, I.W. Satellite-based measurements of surface deformation reveal fluid flow associated with the geological storage of carbon dioxide. *Geophys. Res. Lett.* **2010**, *37*, L03303. [CrossRef]
19. White, J.A.; Chiaramonte, L.; Ezzedine, S.; Foxall, W.; Hao, Y.; Ramirez, A.; McNab, W. Geomechanical behavior of the reservoir and caprock system at the In Salah CO_2 storage project. *Proc. Natl. Acad. Sci. USA* **2014**, *111*, 8747–8752. [CrossRef]
20. Verdon, J.P.; Kendall, J.-M.; Stork, A.L.; Chadwick, R.A.; White, D.J.; Bissell, R.C. Comparison of geomechanical deformation induced by megatonne-scale CO_2 storage at Sleipner, Weyburn, and In Salah. *Proc. Natl. Acad. Sci. USA* **2013**, *110*, E2762–E2771. [CrossRef]
21. Zoback, M.D.; Gorelick, S.M. Earthquake triggering and large-scale geologic storage of carbon dioxide. *Proc. Natl. Acad. Sci. USA* **2012**, *109*, 10164–10168. [CrossRef]
22. Vilarrasa, V.; Carrera, J. Geologic carbon storage is unlikely to trigger large earthquakes and reactivate faults through which CO_2 could leak. *Proc. Natl. Acad. Sci. USA* **2015**, *112*, 5938–5943. [CrossRef]
23. Cappa, F.; Rutqvist, J. Impact of CO_2 geological sequestration on the nucleation of earthquakes. *Geophys. Res. Lett.* **2011**, *38*, L17313. [CrossRef]

24. Shchipanov, A.; Kollbotn, L.; Encinas, M.; Fjelde, I.; Berenblyum, R. Periodic CO_2 injection for improved storage capacity and pressure management under intermittent CO_2 supply. *Energies* **2022**, *15*, 566. [CrossRef]
25. Rahman, M.J.; Fawad, M.; Mondol, N.H. 3D field-scale geomechanical modeling of potential CO_2 storage site Smeaheia, offshore Norway. *Energies* **2022**, *15*, 1407. [CrossRef]
26. Gassnova. *Smeaheia CO_2 Storage Prospect Reference Dataset*; NIRD RDA: Trondheim, Norway, 2021; Version 1. [CrossRef]
27. Erichsen, E.; Rørvik, K.-L.; Haaberg, K.; Keaney, G. Troll Kystnær—Subsurface Status Report; Document TL02-ROS-Z-RA-0005, Revision 03; ROSS Offshore, 2012; pp. 46, 51, 56, 62–63. Available online: https://ccsnorway.com/app/uploads/sites/6/2019/09/tl02-ros-z-ra-0005-troll-kystnaer-subsurface-status-report-rev03.pdf (accessed on 10 October 2026).
28. Wang, Z.; Qi, S.; Zheng, B. Uncertainty analysis of the storage efficiency factor for CO_2 saline resource estimation. *Energies* **2024**, *17*, 1297. [CrossRef]
29. Lee, S.-Y.; Mohamed, F.R.; Lee, K.-H.; McPherson, B.; Balch, R.; Yoon, S. Probabilistic evaluation of geomechanical risks in CO_2 storage: An exploration of caprock integrity metrics using a multilaminate model. *Energies* **2023**, *16*, 6954. [CrossRef]
30. Nowakowski, A. The influence of rate of change in confining and pore pressure on values of the modulus of compressibility of the rock skeleton and Biot's coefficient. *Energies* **2021**, *14*, 3056. [CrossRef]
31. Giani, G.; Orsatti, S.; Peter, C.; Rocca, V. A coupled fluid flow–geomechanical approach for subsidence numerical simulation. *Energies* **2018**, *11*, 1804. [CrossRef]
32. Wei, C.; Wang, L.; Li, B.; Xiong, L.; Liu, S.; Zheng, J.; Hu, S.; Song, H. A study of nonlinear elasticity effects on permeability of stress sensitive shale rocks using an improved coupled flow and geomechanics model: A case study of the Longmaxi Shale in China. *Energies* **2018**, *11*, 329. [CrossRef]
33. Rasmussen, A.F.; Sandve, T.H.; Bao, K.; Lauser, A.; Hove, J.; Skaflestad, B.; Klöfkorn, R.; Blatt, M.; Rustad, A.B.; Sævareid, O.; et al. The Open Porous Media Flow reservoir simulator. *Comput. Math. Appl.* **2021**, *81*, 159–185. [CrossRef]
34. Nordbotten, J.M.; Keilegavlen, E. Two-point stress approximation: A simple and robust finite volume method for linearized (poro-)mechanics and Stokes flow. *arXiv* **2024**, arXiv:2405.10390.
35. Boon, W.M.; Gasda, S.; Sandve, T.H.; Tveit, S. Solving Biot poroelasticity by coupling OPM Flow with the two-point stress approximation finite volume method. *arXiv* **2025**, arXiv:2510.23432.
36. Lee, Y.; Song, I.; Park, C. Analytical assessment of CO_2-storage efficiency and geomechanical-coupling behaviors using poromechanical experiments. *Int. J. Rock Mech. Min. Sci.* **2025**, *196*, 106320. [CrossRef]
37. Chen, M.; Lai, Z.; Kang, Y.; Fang, S.; Liu, H.; Wang, W.; Shen, J.; Chen, Z. Investigation of stress sensitivity of shale nanopores via a nuclear magnetic resonance method. *Energies* **2023**, *16*, 138. [CrossRef]
38. Yao, L.; Lei, Q.; Yang, Z.; He, Y.; Li, H.; Zhao, G.; Zheng, Z.; Hou, H.; Du, M.; Cheng, L. Online nuclear magnetic resonance analysis of the effect of stress changes on the porosity and permeability of shale oil reservoirs. *Energies* **2023**, *16*, 1139. [CrossRef]
39. Qiu, X.; Liu, H.; Liu, M.; Mao, H.; Wang, D.; Ying, Q.; Ban, S. Pore structure evolution in sandstone of underground gas storage during cyclic injection and production based on nuclear magnetic resonance technology. *Energies* **2023**, *16*, 2096. [CrossRef]
40. Skempton, A.W. The consolidation of clays by gravitational compaction. *Q. J. Geol. Soc.* **1969**, *125*, 373–411. [CrossRef]
41. Olson, R.E.; Mesri, G. Mechanisms controlling compressibility of clays. *J. Soil Mech. Found. Div.* **1970**, *96*, 1863–1878. [CrossRef]
42. Burland, J.B. On the compressibility and shear strength of natural clays. *Géotechnique* **1990**, *40*, 329–378. [CrossRef]
43. Vasseur, G.; Djeran-Maigre, I.; Grunberger, D.; Rousset, G.; Tessier, D.; Velde, B. Evolution of structural and physical parameters of clays during experimental compaction. *Mar. Pet. Geol.* **1995**, *12*, 941–954. [CrossRef]
44. Dewhurst, D.N.; Aplin, A.C.; Sarda, J.-P.; Yang, Y. Compaction-driven evolution of porosity and permeability in natural mudstones: An experimental study. *J. Geophys. Res. Solid Earth* **1998**, *103*, 651–661. [CrossRef]
45. Mondol, N.H.; Bjørlykke, K.; Jahren, J.; Høeg, K. Experimental mechanical compaction of clay mineral aggregates—Changes in physical properties of mudstones during burial. *Mar. Pet. Geol.* **2007**, *24*, 289–311. [CrossRef]
46. Yang, Y.; Aplin, A.C. A permeability–porosity relationship for mudstones. *Mar. Pet. Geol.* **2010**, *27*, 1692–1697. [CrossRef]
47. Casey, B.; Germaine, J.T.; Flemings, P.B.; Fahy, B.P. Estimating horizontal stresses for mudrocks under one-dimensional compression. *Mar. Pet. Geol.* **2015**, *65*, 178–186. [CrossRef]
48. Casey, B.; Reece, J.S.; Germaine, J.T. One-dimensional normal compression laws for resedimented mudrocks. *Mar. Pet. Geol.* **2019**, *103*, 397–403. [CrossRef]
49. Dessouki, M.; Hathon, L.; Myers, M. Permeability and porosity modelling for resedimented mudrocks—Applications for compaction dominated mudrock systems. *Mar. Pet. Geol.* **2021**, *128*, 104945. [CrossRef]
50. Uyeturk, C.E.; Germaine, J.T. A general model for the compression of mudrocks. *Mar. Pet. Geol.* **2025**, *174*, 107327. [CrossRef]
51. Uyeturk, C.E.; Germaine, J.T.; Plumb, R. Laboratory characterization of secondary compression behavior of three mudrocks from 1 to 100 MPa effective stress. *Geotech. Test. J.* **2025**, *48*, 942–955. [CrossRef]
52. Kaewhanam, N.; Chaimoon, K. A simplified silty sand model. *Appl. Sci.* **2023**, *13*, 8241. [CrossRef]

53. Phonchamni, N.; Chatwong, T.; Udomchai, A.; Sultornsanee, S.; Angkawisittpan, N.; Sangiamsak, N.; Kaewhanam, N. Refined consolidation settlement calculation based on the oedometer tests for normally and overconsolidated clays. *Appl. Sci.* **2025**, *15*, 5777. [CrossRef]
54. Chatwong, T.; Kaewhanam, N.; Kampala, A.; Eua-apiwatch, S.; Sultornsanee, S. AJOP-T: A high-order hardening law for continuous teardrop bounding surface plasticity. *Mathematics* **2026**, *14*, 2975. [CrossRef]
55. Bhandari, A.R.; Ewy, R.T.; Flemings, P.B.; Germaine, J.T. Comparing compression and shear behavior of intact and resedimented mudrock to illuminate the rheology of mudrocks. In Proceedings of the 58th U.S. Rock Mechanics/Geomechanics Symposium, Golden, CO, USA, 23–26 June 2024; Paper ARMA-2024-1042. [CrossRef]
56. Karig, D.E.; Ask, M.V.S. Geological perspectives on consolidation of clay-rich marine sediments. *J. Geophys. Res. Solid Earth* **2003**, *108*, 2197. [CrossRef]
57. Hurvich, C.M.; Tsai, C.-L. Regression and time series model selection in small samples. *Biometrika* **1989**, *76*, 297–307. [CrossRef]
58. Raue, A.; Kreutz, C.; Maiwald, T.; Bachmann, J.; Schilling, M.; Klingmüller, U.; Timmer, J. Structural and practical identifiability analysis of partially observed dynamical models by exploiting the profile likelihood. *Bioinformatics* **2009**, *25*, 1923–1929. [CrossRef]
59. Shi, Z.; Driba, D.L.; Lopez Rivera, N.; Kariminasab, M.; Beckingham, L.E. A review of coupled geochemical–geomechanical impacts in subsurface CO_2, H_2, and air storage systems. *Energies* **2024**, *17*, 2928. [CrossRef]
60. Reece, J.S.; Flemings, P.B.; Germaine, J.T. Data report: Permeability, compressibility, and microstructure of resedimented mudstone from IODP Expedition 322, Site C0011. *Proc. IODP* **2013**, *322*. [CrossRef]
61. Hüpers, A.; Kopf, A.J. Data report: Consolidation properties of silty claystones and sandstones sampled seaward of the Nankai Trough subduction zone, IODP Sites C0011 and C0012. *Proc. IODP* **2012**, *322*. [CrossRef]
62. Scott, W.; Reece, J.S. The influence of diatoms on hydromechanical properties of marine sediments. *Geochem. Geophys. Geosyst.* **2025**, *26*, e2024GC012064. [CrossRef]
63. Scott, W.; Reece, J.S. *The Influence of Diatoms on Hydromechanical Properties of Marine Sediments*; Version 2; Zenodo: Geneva, Switzerland, 2024. [CrossRef]
64. Casey, B. The Consolidation and Strength Behavior of Mechanically Compressed Fine-Grained Sediments. Ph.D. Thesis, Massachusetts Institute of Technology, Cambridge, MA, USA, 2014. Available online: https://hdl.handle.net/1721.1/90039 (accessed on 10 October 2026).
65. Soldal, M.; Skurtveit, E.; Choi, J.C. Laboratory evaluation of mechanical properties of Draupne shale relevant for CO_2 seal integrity. *Geosciences* **2021**, *11*, 244. [CrossRef]
66. Soldal, M. *Replication Data for: Laboratory Evaluation of Mechanical Properties of Draupne Shale Relevant for CO_2 Seal Integrity*; DataverseNO: Tromsø, Norway, 2023; V1. [CrossRef]
67. Roscoe, K.H.; Burland, J.B. On the generalized stress–strain behaviour of "wet" clay. In *Engineering Plasticity*; Heyman, J., Leckie, F.A., Eds.; Cambridge University Press: London, UK, 1968; pp. 535–609.
68. Pestana, J.M.; Whittle, A.J. Formulation of a unified constitutive model for clays and sands. *Int. J. Numer. Anal. Methods Geomech.* **1999**, *23*, 1215–1243. [CrossRef]
69. Schwarz, G. Estimating the dimension of a model. *Ann. Stat.* **1978**, *6*, 461–464. [CrossRef]
70. Akai, T.; Saito, N.; Hiyama, M.; Okabe, H. Numerical modelling on CO_2 storage capacity in depleted gas reservoirs. *Energies* **2021**, *14*, 3978. [CrossRef]

Disclaimer/Publisher's Note: The statements, opinions and data contained in all publications are solely those of the individual author(s) and contributor(s) and not of MDPI and/or the editor(s). MDPI and/or the editor(s) disclaim responsibility for any injury to people or property resulting from any ideas, methods, instructions or products referred to in the content.